

# Cosmological simulation in tides: power spectrum and halo shape responses, and shape assembly bias

Kazuyuki Akitsu,<sup>a</sup> Yin Li<sup>b</sup> and Teppei Okumura<sup>c,a</sup>

<sup>a</sup>Kavli Institute for the Physics and Mathematics of the Universe (WPI), UTIAS, The University of Tokyo, Kashiwa, Chiba 277-8583, Japan

<sup>b</sup>Center for Computational Astrophysics & Center for Computational Mathematics, Flatiron Institute, 162 5th Avenue, New York, NY 10010, USA

<sup>c</sup>Institute of Astronomy and Astrophysics, Academia Sinica, Roosevelt Road, Taipei 10617, Taiwan, ROC

E-mail: [kazuyuki.akitsu@ipmu.jp](mailto:kazuyuki.akitsu@ipmu.jp), [yinli@flatironinstitute.org](mailto:yinli@flatironinstitute.org), [tokumura@asiaa.sinica.edu.tw](mailto:tokumura@asiaa.sinica.edu.tw)

**Abstract.** The well-developed separate universe technique enables accurate calibration of the response of any observable to an isotropic long-wavelength density fluctuation. The large-scale environment also hosts tidal modes that perturb all observables anisotropically. As in the separate universe, both the long tidal and density modes can be absorbed by an effective anisotropic background, on which the interaction and evolution of the short modes change accordingly. We further develop the tidal simulation method, including proper corrections to the second order Lagrangian perturbation theory (2LPT) to generate initial conditions of the simulations. We measure the linear tidal responses of the matter power spectrum, at high redshift from our modified 2LPT, and at low redshift from the tidal simulations. Our results agree qualitatively with previous works, but exhibit quantitative differences in both cases. We also measure the linear tidal response of the halo shapes, or the shape bias, and find its universal relation with the linear halo bias, for which we provide a fitting formula. Furthermore, analogous to the assembly bias, we study the secondary dependence of the shape bias, and discover for the first time dependence on halo concentration and axis ratio. Our results provide useful insights for studies of the intrinsic alignment as source of either contamination or information. These effects need to be correctly taken into account when one uses intrinsic alignments of galaxy shapes as a precision cosmological tool.

---

## Contents

<b>1</b>	<b>Introduction</b>	<b>1</b>
<b>2</b>	<b>Methodology</b>	<b>3</b>
2.1	Model uniform tidal field by coordinate transformation	3
2.2	Lagrangian perturbation theory and initial conditions	5
2.3	Particle-mesh and tree forces	8
2.4	Time integration	9
<b>3</b>	<b>Simulations</b>	<b>10</b>
<b>4</b>	<b>Results</b>	<b>12</b>
4.1	Power spectrum responses	12
4.1.1	Responses at high redshifts from 2LPT	14
4.1.2	Responses at low redshifts from $N$ -body	15
4.2	Halo shape response	16
4.2.1	Convergence on the resolution and external tides	18
4.2.2	Redshift-dependence: the relation between $b_K$ and $b_1^E$	18
4.2.3	Secondary halo shape responses	19
<b>5</b>	<b>Discussion</b>	<b>20</b>
<b>A</b>	<b>Solving DC density mode at second order</b>	<b>23</b>
<b>B</b>	<b>Second order Lagrangian perturbation theory in an anisotropic background</b>	<b>23</b>
<b>C</b>	<b>Force computation</b>	<b>25</b>
<b>D</b>	<b>Comparison between our simulation and the conventional separate universe simulation</b>	<b>26</b>
D.1	Recap of the usual separate universe simulations	26
D.2	Power spectrum response	27
D.2.1	Convergence of $N$ -body results	28
D.2.2	On the valid scale of our 2LPT at high redshifts	28
D.3	Linear bias	28
<b>E</b>	<b>Results from the inertial tensor <math>I_{ij}</math></b>	<b>28</b>

---

## 1 Introduction

In large-scale structure (LSS) surveys, what we expect to observe is the long-range correlation of biased tracers (e.g. galaxy number density field) mediated by long-wavelength perturbations. Long-wavelength perturbations have an impact on the formation and evolution of the small-scale structure via nonlinear mode-couplings induced by gravity. Because of the equivalence principle, the leading-order effects of the long-wavelength gravitational potential on the local physics arise from the second derivative of the gravitational potential, which can be decomposed

into the large-scale overdensity and tidal fields. Therefore, it has been a fundamental task of LSS cosmology to investigate how large-scale overdensity and tidal fields generate the long-range correlation of biased tracers.

The separate universe simulations provide us with a powerful means to accurately measure or calibrate the local response of various statistics, such as the power spectrum and halo mass function, to the large-scale overdensity field [1–5]. The homogeneity and isotropy of the large-scale overdensity field leads to the simple prescription for the modification, i.e., just changing the cosmological parameters according to the amplitude of the local overdensity. On the other hand, large-scale tidal field breaks isotropy and thus the local background embedded into the large-scale tides is no longer the Friedmann–Lemaître–Robertson–Walker (FLRW) universe but becomes rather anisotropic [6, 7]. Recently there has appeared some works that incorporate the large-scale tidal field in  $N$ -body simulations by introducing anisotropic scale factors [8–11]. This simulation enables us to isolate the effects of the large-scale tidal field since we can impose homogeneous tides in the entire simulation box. In other words, utilizing this simulations we can robustly measure tidal responses separately from other effects.

In this paper, we also implement the large-scale tidal field in a  $N$ -body simulation together with the appropriate initial condition generator where we solve the second order Lagrangian perturbation theory (2LPT) in an anisotropic background. Using our simulations, we measure the two kinds of tidal responses: the matter power spectrum response and the halo shape response. The large-scale tidal field makes the the local clustering pattern anisotropic, which potentially mimics other anisotropic signature such as redshift-space distortion and Alcock-Paczyński effects [12–14]. The tidal response of the matter power spectrum measured from our simulations can give a rough estimate of such contaminants on small scales. The response also allows us to compute the covariance of weak lensing power spectra [15]. Since no conclusive results have yet been reached about the amplitude or scale-dependence of the tidal response of the matter power spectrum at high redshifts due to possible numerical artifacts [9, 11], we show the tidal response of the matter power spectrum from our modified 2LPT.

The density field is not the only ones affected by the large-scale tidal field; the shape of galaxies and halos is naturally affected as well. Indeed, shapes of galaxy or halos even at large separation are aligned with each other due to the large-scale tidal field, known as “intrinsic alignments” [16–18]. The intrinsic alignments are usually considered as a source of error in measuring weak lensing signals from galaxy imaging surveys. However, given that their origin is the underlying large-scale tidal field, they should have their own cosmological information. For example, the intrinsic alignments potentially probe the energy budget of the universe [19, 20], the stochastic gravitational waves background [21, 22], and the angular-dependent primordial non-Gaussianity [23–25]. In order to extract the cosmological information from measurements of intrinsic alignments, it is of importance to test the theoretical model of the intrinsic alignments. Our simulation allows us to directly examine the most simple model of the intrinsic alignment, so-called linear alignment or tidal alignment model [16, 17], which predicts shapes of galaxy or halo are linearly aligned with the large-scale tides. Using well-controlled tidal simulations, we quantify the strength of the alignments over wide redshift and mass range and explore the secondary dependence of the alignment strength on halo properties other than halo mass.

This paper is laid out as follows. In Section 2, we present how to absorb the large-scale tidal and density fields into the simulation background and modifications of the 2LPT initial condition in anisotropic background. Section 3 summarize our simulation specifications. In

Section 4, we show results on both the tidal response of the matter power spectrum and the halo shapes. We give conclusion and discussion in Section 5. Appendices A-C provide the details of computation and our modifications. We show the convergence test of our simulations by comparing ours with the usual separate universe simulations in Appendix D. Results of the different shape definition used in the main text are summarized in Appendix E.

## 2 Methodology

A uniform (DC) tidal or density field preserves the translational symmetry, and can be modeled effectively as a time-dependent coordinate transformation. By doing this, we separate out the DC modes, and absorb it including its evolution into an effective background, which we can include in  $N$ -body simulations [26]. In this section we present analytical derivations and numerical implementations of this method. Many of the results have already been obtained in the recent literature [9]. Here we simplify the derivations, and present for the first time the modulation of the tidal modes on the second order Lagrangian perturbation theory (2LPT).

### 2.1 Model uniform tidal field by coordinate transformation

In Newtonian cosmology, the large-scale effect of infinitely long-wavelength (i.e. DC) density and tidal modes on a dark matter particle can be absorbed by a coordinate transformation

$$\mathbf{r}_i = a_{ij} \mathbf{x}_j, \quad (2.1)$$

where  $\mathbf{r}$  is the physical coordinate of the dark matter particle, and  $a_{ij}$  is a symmetric matrix that absorbs the DC modes so that the large-scale displacement is isotropic in the  $\mathbf{x}$  coordinate. We normalize  $a_{ij}$  to the scale factor of global expansion  $a \delta_{ij}$  in the absence of any DC-mode, in which case  $\mathbf{x}$  reduces to the usual comoving coordinates.

From Eq. (2.1) we can immediately separate the physical velocity  $u_i$  into the expansion of a local background and a peculiar component.

$$u_i \equiv \dot{r}_i = H_{ij} r_j + v_i, \quad (2.2)$$

where the overdot denotes a time derivative,  $H_{ij} \equiv \dot{a}_{ik} [a^{-1}]_{kj}$  describes a local anisotropic Hubble expansion, and  $v_i \equiv a_{ij} \dot{x}_j$  is the peculiar velocity.

The dark matter particles follow the Newtonian equation of motion

$$\dot{u}_i = -\frac{\partial}{\partial r_i}(\Phi + \phi), \quad (2.3)$$

where we split the gravitational potential into an effective background potential  $\Phi$  and a peculiar potential  $\phi$ . By plugging Eq. (2.2) into Eq. (2.3), we see that the acceleration also splits into a local background expansion and a peculiar piece, which are respectively driven by  $\Phi$  and  $\phi$ ,

$$\ddot{a}_{ik} [a^{-1}]_{kj} r_j = -\partial \Phi / \partial r_i, \quad (2.4)$$

$$\dot{v}_i + H_{ij} v_j = -\partial \phi / \partial r_i. \quad (2.5)$$

One can regard Eq. (2.4) as a modified Friedmann equation. The large-scale stress due to the DC modes is absorbed into  $\Phi$ , leaving  $\phi$  sourced only by the local structures,

$$\nabla_{\mathbf{r}}^2 \phi = 4\pi G \bar{\rho}_m (1 + \Delta_0) \delta, \quad (2.6)$$

where  $\bar{\rho}_m$  is the mean density of matter,  $\Delta_0$  is the large-scale overdensity relative to  $\bar{\rho}_m$ , and  $\delta$  denotes the overdensity with respect to the local background density  $\bar{\rho}_m(1 + \Delta_0)$ . Mass conservation between  $a \rightarrow 0$  and a later time requires  $\bar{\rho}_m(1 + \Delta_0)d^3\mathbf{r} = \bar{\rho}_ma^3d^3\mathbf{x}$ , or

$$1 + \Delta_0 \equiv \frac{a^3}{\det a_{ij}}. \quad (2.7)$$

Without loss of generality, we can simplify the equations and the numerical implementation by rotating the simulation box to align with the principal axes of the DC tides, so that  $a_{ij} = a_i\delta_{ij}$  and  $H_{ij} = H_i\delta_{ij} = \dot{a}_i\delta_{ij}/a_i$  with their off-diagonal degrees of freedom eliminated. Let us define  $\Delta_i$  as the relative difference of  $a_i$  to  $a$ :

$$1 + \Delta_i \equiv \frac{a_i}{a}, \quad i = 1, 2, 3. \quad (2.8)$$

Combining the above two equations implies mass conservation,

$$(1 + \Delta_0)(1 + \Delta_1)(1 + \Delta_2)(1 + \Delta_3) = 1. \quad (2.9)$$

We also have

$$H_i = H + \frac{\dot{\Delta}_i}{1 + \Delta_i} \simeq H + \dot{\Delta}_i, \quad (2.10)$$

where  $H$  is the global expansion rate. The approximation holds at high redshifts when  $\Delta_i \ll 1$ .

This rotation also diagonalizes the DC tidal field, the traceless part of the Hessian of the large-scale potential, to  $\tau_{ij} = \tau_i\delta_{ij}$ . Now we can write down the effective background potential that absorbs the DC density and tidal modes

$$\Phi = \frac{2}{3}\pi G\bar{\rho}_m(1 + \Delta_0)r^2 - \frac{\Lambda}{6}r^2 + 2\pi G\bar{\rho}_m\tau_i r_i^2. \quad (2.11)$$

The DC density modulation  $1 + \Delta_0$  is determined through Eq. (2.7), and the last term is sourced by the DC tidal mode. One can easily verify that substituting the first two terms without  $\Delta_0$  into Eq. (2.4) gives rise to the usual Friedmann equation.

To determine the evolution of  $\Delta_i$  in the presence of  $\tau_i$ , we plug Eq. (2.11) into Eq. (2.4) and subtract the usual Friedmann equation, then it reads

$$\ddot{\Delta}_i + 2H\dot{\Delta}_i = -4\pi G\bar{\rho}_m \left( \tau_i + \frac{1}{3}\Delta_0 \right) (1 + \Delta_i). \quad (2.12)$$

Note the addition of  $\Delta_0$  in Eq. (2.11) is valid even at nonlinear level. This can be verified by setting  $\tau_i = 0$  to reproduce evolution of the spherical collapse model (e.g. [2]). For anisotropic simulations we compute the anisotropic scale factor in the following subsections by solving Eq. (2.12) and Eq. (2.9) numerically, using matter dominated initial conditions.

Before proceeding to the next subsection, we can derive some analytic solutions for better understanding. Linearizing Eq. (2.12) drops the  $1 + \Delta_i$  factor on the right hand side, and yields an equation with the same form as that of the linear growth function  $D$ , if we replace  $-(\tau_i + \Delta_0/3)$  with  $\Delta_i$ . Because both  $\tau_i$  and  $\Delta_0$  are proportional to  $D$ , the linear-order solution is simply given by

$$\Delta_i^{(1)} = -\tau_i - \frac{\Delta_0^{(1)}}{3}. \quad (2.13)$$

Unsurprisingly, the linear anisotropic correction to the scale factor is the sum of the isotropic one  $-\Delta_0^{(1)}/3$  and the tidal mode. Summing over  $i$  and using the traceless constraint  $\sum_i \tau_i = 0$ , one can verify

$$\Delta_0^{(1)} + \sum_i \Delta_i^{(1)} = 0, \quad (2.14)$$

which is equivalent to Eq. (2.9) in the linear theory limit.

The linear tide  $\tau_i$  also induces the correct second order overdensity. We derive the second order solution for  $\Delta_0$  in App. A, and show here the solution for the matter dominated era,

$$\Delta_0^{(2)} = \frac{5}{7}\Delta_0^{(1)2} + \frac{2}{7}\sum_i \Delta_i^{(1)2} = \frac{17}{21}\Delta_0^{(1)2} + \frac{2}{7}\sum_i \tau_i^2. \quad (2.15)$$

This is consistent with the result from second-order standard perturbation theory (e.g. [27]).

## 2.2 Lagrangian perturbation theory and initial conditions

Due to gravity, the long-wavelength modes are coupled to the short ones and affect their growth. Here we solve the leading-order anisotropic perturbations to the first and second order Lagrangian displacement, and use the results to generate initial conditions for the  $N$ -body simulations. The long modes  $\Delta_0$  and  $\Delta_i$  are assumed to be first order in the following derivations.

The Lagrangian perturbation theory follows the evolution of the displacement field  $\Psi(\mathbf{q})$ , a mapping from a particle's Lagrangian position  $\mathbf{q}$  to its Eulerian position  $\mathbf{x}$ :

$$x_i = q_i + \Psi_i(\mathbf{q}). \quad (2.16)$$

Before shell crossing, the overdensity is simply related to its Jacobian determinant by

$$\delta = \left| \frac{\partial \mathbf{x}}{\partial \mathbf{q}} \right|^{-1} - 1 = |\delta_{ij} + \Psi_{i,j}|^{-1} - 1, \quad (2.17)$$

where  $\Psi_{i,j} \equiv \partial \Psi_i / \partial q_j$ .

To derive the master equation of the Lagrangian perturbation theory, we substitute Eq. (2.16) into Eq. (2.5),

$$\ddot{\Psi}_i^{(1)} + 2 \sum_i H_i \dot{\Psi}_i^{(1)} = - \sum_i \frac{1}{a_i} \frac{\partial \phi}{\partial r_i}. \quad (2.18)$$

Taking the derivative with respect to  $x_i$  and then summing over  $i$ , we obtain the master equation

$$\sum_{ij} \left| \frac{\partial \mathbf{x}}{\partial \mathbf{q}} \right| [\delta_{ij} + \Psi_{i,j}]^{-1} [\ddot{\Psi}_{i,j} + 2H_i \dot{\Psi}_{i,j}] = 4\pi G \bar{\rho}_m (1 + \Delta_0) \left( \left| \frac{\partial \mathbf{x}}{\partial \mathbf{q}} \right| - 1 \right), \quad (2.19)$$

where we have used Eq. (2.6) and Eq. (2.17), and the chain rule  $\partial/\partial x_i = [\partial q_j / \partial x_i] \partial/\partial q_j$ .

Now let us start with the Zel'dovich approximation (ZA; linear Lagrangian perturbation theory [28]). Keeping only the leading order displacement terms in Eq. (2.19) leads to

$$\sum_i \ddot{\Psi}_{i,i}^{(1)} + 2 \sum_i H_i \dot{\Psi}_{i,i}^{(1)} = \frac{3}{2} H^2 \Omega_m(a) (1 + \Delta_0) \sum_i \Psi_{i,i}^{(1)}. \quad (2.20)$$

In deriving the above equation we have used  $|\partial\mathbf{x}/\partial\mathbf{q}|^{-1} \simeq 1 + \sum_i \Psi_{i,i}$  and  $\Omega_m(a) \equiv \bar{\rho}_m/\rho_c = 8\pi G\bar{\rho}_m/3H^2$ , with  $\rho_c$  being the critical density.

At linear order the vorticity in  $\Psi_{i,j}^{(1)}$  decays, so the growing displacement solution is a potential flow  $\Psi_i^{(1)} = -\partial\psi_W^{(1)}/\partial q_i \equiv -\dot{\psi}_{W,i}^{(1)}$ , with the potential  $\psi_W^{(1)}$  sourced by the overdensity in Lagrangian space:

$$\nabla_{\mathbf{q}}^2 \psi_W^{(1)} \equiv \sum_i \psi_{W,ii}^{(1)} = \delta^{(1)}. \quad (2.21)$$

In terms of  $\psi_W^{(1)}$ , (2.20) is

$$\sum_i \ddot{\psi}_{W,ii}^{(1)} + 2 \sum_i H_i \dot{\psi}_{W,ii}^{(1)} - \frac{3}{2} \Omega_m(a) (1 + \Delta_0) \sum_i \psi_{W,ii}^{(1)} = 0. \quad (2.22)$$

The subscript  $W$  here denotes local quantities inside a *window*, within which the DC density and tidal modes can be nonzero.

This is in contrast with the usual linear growth equation, which describes the evolution of the short modes in the global background where the long modes vanish. It can be obtained by setting  $H_i \rightarrow H$  and  $\Delta_0 \rightarrow 0$  in the above equation,

$$\sum_i \ddot{\psi}_{ii}^{(1)} + 2H \sum_i \dot{\psi}_{ii}^{(1)} - \frac{3}{2} H^2 \Omega_m(a) \sum_i \psi_{ii}^{(1)} = 0. \quad (2.23)$$

The solution to this equation gives the usual time dependence by the linear growth function,  $\psi^{(1)} \propto D(t)$ .

In the presence of the long modes, the displacement potential  $\psi_W^{(1)}$  receives corrections of order  $\mathcal{O}(\psi^{(1)}\Delta)$ . We denote this correction as  $\epsilon^{(1)}$  so that the solution of Eq. (2.22) can be written as

$$\psi_W^{(1)} = \psi^{(1)} + \epsilon^{(1)}. \quad (2.24)$$

Then using Eq. (2.10), Eq. (2.22), and Eq. (2.23) one can show that  $\epsilon^{(1)}$  satisfies

$$\sum_i \ddot{\epsilon}_{,ii}^{(1)} + 2H \sum_i \dot{\epsilon}_{,ii}^{(1)} - \frac{3}{2} H^2 \Omega_m(a) \sum_i \epsilon_{,ii}^{(1)} = -2 \sum_i \dot{\psi}_{,ii}^{(1)} \dot{\Delta}_i + \frac{3}{2} H^2 \Omega_m(a) \Delta_0 \sum_i \psi_{,ii}^{(1)}. \quad (2.25)$$

We can solve this equation easily by rewriting it in Fourier space

$$\ddot{\epsilon}^{(1)} + 2H\dot{\epsilon}^{(1)} - \frac{3}{2} \Omega_m(a) \epsilon^{(1)} = -2\dot{\psi}^{(1)} \sum_i \hat{p}_i^2 \dot{\Delta}_i + \frac{3}{2} H^2 \Omega_m(a) \psi^{(1)} \Delta_0. \quad (2.26)$$

Here in this subsection (and App. B) we use  $\mathbf{p}$  to denote the local Lagrangian space wavevector, with  $\hat{\mathbf{p}}$  being its direction. The above equation clearly shows that the effect of the long modes manifests in the quadrupolarly direction-dependent Hubble drag, whose coefficients depend on the growth history of the long modes  $\Delta_i(t)$ .

To solve the above equation we can first decompose it as

$$\epsilon^{(1)}(a, \hat{\mathbf{p}}) = \sum_i \hat{p}_i^2 \epsilon_i^{(1)}(a), \quad (2.27)$$

with each component  $\epsilon_i^{(1)}(a)$  satisfying

$$\ddot{\epsilon}_i^{(1)} + 2H\dot{\epsilon}_i^{(1)} - \frac{3}{2} \Omega_m(a) \epsilon_i^{(1)} = -2\dot{\psi}^{(1)} \dot{\Delta}_i + \frac{3}{2} H^2 \Omega_m(a) \psi^{(1)} \Delta_0. \quad (2.28)$$

Note that  $\epsilon_i^{(1)}$  here is different from  $\epsilon_{,ii}^{(1)}$  in Eq. (2.25). For matter dominated era, assuming that  $H = 2/3t$ ,  $\Omega_m(a) = 1$ , and the long modes are well sub-horizon ( $\Delta_0, \Delta_i \propto D^{(1)}$ ), we obtain

$$\epsilon_i^{(1)} = -\frac{4}{7}\Delta_i\psi^{(1)} + \frac{3}{7}\Delta_0\psi^{(1)}. \quad (2.29)$$

Now we can write down the Fourier-space correction to ZA due to the long modes

$$\epsilon^{(1)} = \psi^{(1)}\left(\frac{3}{7}\Delta_0 - \frac{4}{7}\sum_i \Delta_i \hat{p}_i^2\right). \quad (2.30)$$

This can be understood as a direction-dependent modulation on the linear growth function

$$D_W(t, \hat{\mathbf{p}}) = D(t)\left(1 + \frac{3}{7}\Delta_0 - \frac{4}{7}\sum_i \Delta_i \hat{p}_i^2\right), \quad (2.31)$$

where  $D_W(t, \hat{\mathbf{p}})$  is the modified linear growth function for a Fourier mode along  $\hat{\mathbf{p}}$ . Eq. (2.31) can be directly compared to the results derived with standard perturbation theory in an Einstein de-Sitter universe. For isotropic perturbation,  $\Delta_i = -\Delta_0/3$ , so  $D_W^{(1)} = D^{(1)}(1 + 13\Delta_0/21)$  and for pure tides,  $\Delta_0 = 0$  and  $\Delta_i = -\tau_i$ , so  $D_W^{(1)} = D^{(1)}(1 + 4\sum_i \tau_i \hat{p}_i^2/7)$ .

The above derivations have shown that the tidal effect on ZA is simpler in Fourier space, and can be captured by a direction-dependent modulation on the linear growth function. However, this is not the case for 2LPT, for which we find the correction more straightforward in the configuration space. Again we define the second order displacement potential and its correction by  $\psi_W^{(2)} = \psi^{(2)} + \epsilon^{(2)}$ . For the matter dominated era, we find the following solution

$$\begin{aligned} \sum_i \epsilon_{,ii}^{(2)}(t, \mathbf{q}) = & \frac{1}{4} \left[ -\frac{16}{9} \sum_i \psi_{,ii}^{(2)}(t, \mathbf{q}) \Delta_i + \frac{8}{9} \sum_{ij} \psi_{,ij}^{(1)}(t, \mathbf{q}) \psi_{,ji}^{(1)}(t, \mathbf{q}) \Delta_i \right] \\ & + \frac{1}{6} \left[ \sum_i \psi_{,ii}^{(2)} - \frac{1}{2} \sum_i \left( \psi_{,ii}^{(1)} \right)^2 - \frac{1}{2} \sum_{ij} \psi_{,ij}^{(1)} \psi_{,ji}^{(1)} \right] \Delta_0 \\ & + \frac{1}{4} \left[ -\frac{2}{3} \sum_i \psi_{,ii}^{(1)}(t, \mathbf{q}) \sum_j \epsilon_{,jj}^{(1)}(t, \mathbf{q}) + \frac{20}{9} \sum_{ij} \psi_{,ij}^{(1)}(t, \mathbf{q}) \epsilon_{,ij}^{(1)}(t, \mathbf{q}) \right]. \end{aligned} \quad (2.32)$$

We present the general formula and its derivation in App. B.

Having derived the leading order perturbations to ZA and 2LPT by the DC modes, we can implement them numerically to generate initial conditions for our tidal simulations. We modify the initial condition code 2LPTIC [29] to include the  $\epsilon^{(1)}$  and  $\epsilon^{(2)}$  corrections to the displacements, as well as the corresponding corrections to the initial velocities. Since  $\epsilon^{(1)} \propto D^2$  and  $\epsilon^{(2)} \propto D^3$  during matter domination, the correction to ZA and 2LPT velocities are respectively

$$\begin{aligned} a\dot{\epsilon}_{,i}^{(1)} &= 2Hf_1\epsilon_{,i}^{(1)}, \\ a\dot{\epsilon}_{,i}^{(2)} &= 3Hf_1\epsilon_{,i}^{(2)}. \end{aligned} \quad (2.33)$$

with  $f_1 \equiv d \ln D / d \ln a \simeq [\Omega_m(a)]^{5/9}$ . Since we generate the initial condition at  $a_i$  deep in the matter dominated era, the above approximations should be accurate.



There is one other thing to note about the velocity modifications. Here we derive the correction to the peculiar velocity  $a\dot{\mathbf{x}}$ . However, the series of **Gadget** codes uses the canonical momentum  $\mathbf{P} \equiv a^2 m \dot{\mathbf{x}}$  as the internal velocity variable, and another velocity variable  $\mathbf{u} \equiv \sqrt{a} \dot{\mathbf{x}}$  in their data format when saving and loading data. Therefore, given that we are dealing with anisotropic scale factors, we need to be careful when converting among peculiar velocity, momentum, and velocity variable on disks. We multiplied  $\sqrt{a}\dot{\Psi}_i$  by  $\sqrt{1 + \Delta_i}$  when generating and saving the initial conditions, and then modified the conversion factor  $a\sqrt{a}$  from  $\mathbf{u}$  to  $\mathbf{P}$  as  $a_i\sqrt{a_i}$ , which eventually results in the modified canonical momentum  $P_i = a_i^2 \dot{x}_i$ .

### 2.3 Particle-mesh and tree forces

Because the new effective background evolves anisotropically, the gravitational force and the equation of motion, isotropic in physical coordinates, need to be modified and expressed in the local comoving coordinates. We describe the modification of the force law here, and explain the time integration in the next subsection.

We focus on TreePM method which computes gravitational force efficiently by splitting it into the long-range and short-range contributions, computed by the particle mesh (PM) method and the tree algorithm [30, 31], respectively. The PM forces can be solved efficiently in Fourier space, and the tree forces of nearby particles are summed with the help of a tree data structure. In the absence of the long modes

$$\begin{aligned}\phi &= \phi^{\text{PM}} + \phi^{\text{T}}, \\ \phi^{\text{PM}}(\mathbf{k}) &= -4\pi G \bar{\rho}_{\text{m}} a^2 \frac{\delta(\mathbf{k})}{k^2} e^{-k^2 x_s^2} \\ \phi^{\text{T}}(\mathbf{x}) &= -\frac{Gm}{a} \sum_n \frac{1}{|\mathbf{x} - \mathbf{x}_n|} \text{erfc}\left(\frac{|\mathbf{x} - \mathbf{x}_n|}{2x_s}\right)\end{aligned}\quad (2.34)$$

where  $\mathbf{k}$  is the wavevector,  $\mathbf{x}_n$  denotes the position of the  $n$ -th particle, and the overdensity field is determined by the spatial distribution of the particles

$$\bar{\rho}_{\text{m}}(1 + \delta(\mathbf{x})) = \frac{m}{a^3} \sum_n \delta^{\text{D}}(\mathbf{x} - \mathbf{x}_n). \quad (2.35)$$

The long- and short-range forces in (2.34) are split with a Gaussian kernel of comoving width  $x_s$ . One can verify straightforwardly the above force splitting, using the fact that  $e^{-k^2 x_s^2}/k^2$  and  $\text{erf}(x/2x_s)/4\pi x$  are 3D Fourier transform pair. The acceleration due to the tree force is

$$-\nabla_{\mathbf{x}} \phi^{\text{T}} = -\frac{Gm}{a} \sum_n \frac{\mathbf{x} - \mathbf{x}_n}{|\mathbf{x} - \mathbf{x}_n|^3} \left[ \text{erfc}\left(\frac{|\mathbf{x} - \mathbf{x}_n|}{2x_s}\right) + \frac{|\mathbf{x} - \mathbf{x}_n|}{x_s \sqrt{\pi}} \exp\left(-\frac{|\mathbf{x} - \mathbf{x}_n|^2}{4x_s^2}\right) \right]. \quad (2.36)$$

Now let us modify the above conventional TreePM algorithm for an anisotropically expanding universe. The modified Poisson equation (2.6),

$$(1 + \Delta_i)^{-2} \frac{\partial^2}{\partial x_i^2} \phi = 4\pi G \bar{\rho}_{\text{m}} a^2 (1 + \Delta_0) \delta, \quad (2.37)$$

implies that the TreePM potentials in the presence of the long modes should be

$$\begin{aligned}\phi^{\text{PM}}(\mathbf{p}) &= -4\pi G \bar{\rho}_{\text{m}} a^2 (1 + \Delta_0) \frac{\delta(\mathbf{p})}{k^2} e^{-p^2 x_s^2}, \\ \phi^{\text{T}}(\mathbf{x}) &= -\frac{Gm}{a} \sum_n \frac{a}{|\mathbf{r} - \mathbf{r}_n|} - \phi^{\text{PM}}(\mathbf{x}),\end{aligned}\quad (2.38)$$

where we have introduced  $\mathbf{p}$  as the local comoving wavevector<sup>1</sup>, related to the global comoving wavevector by

$$k_i = \frac{p_i}{1 + \Delta_i}. \quad (2.39)$$

And recall  $r_i = a_i x_i$  is the physical coordinates. As expected, both the PM and tree forces above are manifestly isotropic in the physical or global comoving coordinates. In App. C we provide the functional form of  $\phi^{\text{PM}}(\mathbf{x})$ , which involves integral and no longer has the simple form in Eq. (2.34).

Note that there are two choices on the force-splitting scale: isotropic in physical scales, i.e. anisotropic in local comoving scales, or isotropic in local comoving scales, i.e. anisotropic in physical scales. In the former case the equations become quite simple. However, we have found this choice introduces numerical artifacts, e.g. on the second order responses to tides of the halo abundance. This is probably because in this case the force-splitting boundary in local comoving scales (i.e., the simulation coordinates) is neither isotropic nor constant in time, and can interact with the anisotropic PM force artifacts at grid scales. To avoid this problem we choose to split force isotropically in local comoving scales, following Ref. [9]. The tree acceleration now is

$$-\frac{\partial \phi^{\text{T}}}{\partial x_i} = -\frac{Gm}{a} \sum_n \frac{aa_i [\mathbf{r} - \mathbf{r}_n]_i}{|\mathbf{r} - \mathbf{r}_n|^3} + \frac{\partial \phi^{\text{PM}}}{\partial x_i}. \quad (2.40)$$

Since  $\partial \phi^{\text{PM}} / \partial x_i$  is computationally expensive to exactly evaluate in simulations, we expanded this in terms of  $\Delta_i$  and included up to the second order terms in  $\Delta_i$  as in Ref. [9]. Details are given in App. C.

## 2.4 Time integration

From Eq. (2.5), the equation of motion for the peculiar part takes a simple form of

$$\frac{\dot{P}_i}{m} = -\frac{\partial \phi}{\partial x^i}, \quad (2.41)$$

where  $\mathbf{P} = a^2 m \dot{\mathbf{x}}$  is the canonical momentum of the  $N$ -body Hamiltonian

$$H = \sum_n \frac{\mathbf{P}_n^2}{2ma^2} + \sum_{n \neq n'} \frac{m^2 \varphi(\mathbf{x}_n - \mathbf{x}_{n'})}{2a}, \quad (2.42)$$

in which  $\varphi$  is the potential of a unit-mass particle in a box of comoving size  $L$  at  $a = 1$ :

$$\nabla_{\mathbf{x}}^2 \varphi = 4\pi G \left( \delta^{\text{D}}(\mathbf{x} - \mathbf{x}') - \frac{1}{L^3} \right). \quad (2.43)$$

Note that we have made the time dependence in the potential explicit by introducing  $\varphi$ , which otherwise is simply related to  $\phi$  by Eq. (2.6) and Eq. (2.35).

$N$ -body simulations use the computed gravitational forces to update the particle velocities and then their positions to evolve them in time. This time integration is performed using the

---

<sup>1</sup>Though this Eulerian  $\mathbf{p}$  is technically different from the Lagrangian one in Sec. 2.2, they are both Fourier conjugates to the local comoving coordinates, therefore denoted by the same symbol.

kick and drift leapfrog operators [32, 33]

$$\text{Kick : } \quad \frac{\mathbf{P}}{m} \rightarrow \frac{\mathbf{P}}{m} - \nabla_{\mathbf{x}} \phi \int_t^{t+\Delta t} \frac{dt}{a}, \quad (2.44)$$

$$\text{Drift : } \quad \mathbf{x} \rightarrow \mathbf{x} + \frac{\mathbf{P}}{m} \int_t^{t+\Delta t} \frac{dt}{a^2}. \quad (2.45)$$

On the anisotropic background, the Hamiltonian leading to the modified EoM Eq. (2.41) is

$$H = \sum_n \sum_{i=1}^3 \frac{P_{n,i}^2}{2ma_i^2} + \sum_{n \neq n'} \frac{m^2 \varphi(\mathbf{x}_n - \mathbf{x}_{n'})}{2a}, \quad (2.46)$$

where  $P_{n,i} \equiv a_i^2 m \dot{x}_{n,i}$  are the conjugate momenta of  $x_{n,i}$ . Thus we have

$$\text{Kick : } \quad \frac{\mathbf{P}}{m} \rightarrow \frac{\mathbf{P}}{m} - \nabla_{\mathbf{x}} \phi \int_t^{t+\Delta t} \frac{dt}{a}, \quad (2.47)$$

$$\text{Drift : } \quad x_i \rightarrow x_i + \frac{P_i}{m} \int_t^{t+\Delta t} \frac{dt}{a_i^2}. \quad (2.48)$$

Note that the drift operator changes due to the modified canonical momentum, where as the kick operator is unchanged, with the anisotropic effect on force calculations already accounted for in Sec. 2.3. We implement modifications of the TreePM forces and time integration based on L-Gadget2 [33].

### 3 Simulations

We perform  $N$ -body simulations in the tidal backgrounds as described in the previous section, using the Planck 2015 cosmology [34]:  $\Omega_m = 0.3089$ ,  $\Omega_\Lambda = 0.6911$ ,  $h = 0.6774$ ,  $n_s = 0.9667$ , and  $\sigma_8 = 0.8159$ . We generate initial conditions at redshift  $z_i = 49$  with  $1024^3$  particles using CLASS [35] and our modified 2LPTIC<sup>2</sup>, and then run the modified L-Gadget2 [33] with  $N_{\text{mesh}} = 2048^3$  TreePM grid. To cover a large range of halo masses, we use 3 different box sizes:  $L = 250 \text{ Mpc}/h$ ,  $L = 1 \text{ Gpc}/h$ , and  $L = 3 \text{ Gpc}/h$ .

So far we have used  $\Delta_1$ ,  $\Delta_2$ , and  $\Delta_3$  to parametrize the remaining 3 eigenvalues of the background strain. Alternatively one can parametrize it by 1 isotropic dilation and 2 anisotropic scalings [6], with the former equal to the negative DC overdensity at linear order,

$$\begin{aligned} -\Delta_0^{(1)} &= \Delta_1^{(1)} + \Delta_2^{(1)} + \Delta_3^{(1)} = -(\tau_1 + \tau_2 + \tau_3), \\ \Delta_e &\equiv \frac{\Delta_1^{(1)} - \Delta_2^{(1)}}{2} = -\frac{\tau_1 - \tau_2}{2}, \\ \Delta_p &\equiv \Delta_3^{(1)} - \frac{\Delta_1^{(1)} + \Delta_2^{(1)}}{2} = -\tau_3 + \frac{\tau_1 + \tau_2}{2}. \end{aligned} \quad (3.1)$$

The subscripts of the two anisotropic scaling modes stand for ellipticity and prolaticity<sup>3</sup>.

To focus on the tidal effects, we can remove the linear order overdensity mode by setting  $\Delta_0^{(1)} = 0$ , and run “pure” tidal simulations by perturbing the remaining 2 degrees of freedom,

<sup>2</sup><https://cosmo.nyu.edu/roman/2LPT/>

<sup>3</sup>We do not impose ordering on  $\Delta_i$ ’s to compress the parameter space (cf. [6]).

type of simulations	$\Delta_0^{(1)}$	$\Delta_p$	$\Delta_e$	$L$ [Mpc/h]	$N_p$	realizations
fiducial	0	0	0	250	1024 <sup>3</sup>	6
				1000		
				3000		
$\Delta_0$ -type	$\pm 0.09$	0	0	250		
				1000		
				3000		
$\Delta_p$ -type	0	$\pm 0.15$	0	250		
				1000		
				3000		
$\Delta_e$ -type	0	0	$\pm 0.1$	250		
				1000		
				3000		

**Table 1:** Summary of our 126  $N$ -body simulations, of different types of mean strains (related to the DC density and tidal modes) in the box. The  $\Delta_0$ -type simulations have isotropic strain (DC density perturbations); the  $\Delta_p$ -type and  $\Delta_e$ -type perturb the two DC tidal modes separately as decomposed in Eq. (3.1); and the fiducial type are conventional simulations without DC modes on global background cosmology.  $\Delta_0^{(1)}$ ,  $\Delta_p$ , and  $\Delta_e$  specify the strain amplitudes of their respective types;  $L$  are the simulation box sizes; and  $N_p$  is the total number of particle.

$\Delta_p$  and  $\Delta_e$ . We also vary the 2 modes separately, further dividing those pure tidal simulations into  $\Delta_p$ - and  $\Delta_e$ -type simulations. For  $\Delta_p$ -type simulations we chose the background strain to satisfy  $\Delta_0^{(1)} = 0$  and  $\Delta_e = 0$  so that the remaining degree of freedom is only  $\Delta_p = 3\Delta_3^{(1)}/2$ . For  $\Delta_e$ -type simulations we chose the background strain to satisfy  $\Delta_0^{(1)} = 0$  and  $\Delta_p = 0$  so that the remaining degree of freedom is only  $\Delta_e = \Delta_1^{(1)}$ . This means the configuration of the tides and linear strain take the form  $(\tau_1, \tau_2, \tau_3) = (1, 1, -2)\Delta_p/3$  for  $\Delta_p$ -type simulations, and  $(\tau_1, \tau_2, \tau_3) = (-1, 1, 0)\Delta_e$  for  $\Delta_e$ -type simulations.

Our modification for the tidal background also works for the isotropic configuration, where  $\Delta_p = \Delta_e = 0$  and only  $\Delta_0^{(1)}$  is varied. In fact this configuration is equivalent to the usual isotropic separate universe simulation at the nonlinear level. We validate our simulation pipeline by running the  $\Delta_0$ -type simulations and comparing them to the separate universe simulations. We find their power spectrum responses and halo biases are fully consistent with each other, as summarized in App. D.

As reference and normalization for the response estimations, we also run some conventional fiducial simulations without any variation in the DC density or tidal modes. For each of type of simulations, each box size, and each sign (positive, negative, or fiducial) of the DC modes, we have performed 6 simulations, and in total used 126 simulations to produce our results. Simulations with different DC modes shares the same random phases in the initial conditions so that sample variances in the response functions are suppressed. We summarize all our simulations in Table 1.

## 4 Results

In this section, we present analytic expressions and numerical calibrations of the power spectrum tidal response, including the high-redshift response from 2LPT and low-redshift one from  $N$ -body simulations; we also present measurements of the halo shape response to the tidal field. For the latter, we study its dependence on the halo mass and other (secondary) halo properties, including the concentration and axis ratio. This is analogous to the halo assembly bias, the dependence of halo abundance on variables beyond the halo mass.

### 4.1 Power spectrum responses

The long-wavelength modes modulate the evolution of the short-wavelength ones, in their amplitudes and scales, known as the growth and dilation effects [1], respectively. The growth effect focuses on the changes in short mode amplitude in the local comoving coordinate system, as considered in Sec. 2.2. On the other hand, the dilation effect arises from the (anisotropic) expansion of the local comoving coordinate system with respect to the global one, as described in Sec. 2.1. In addition to the growth and dilation effects, the change in reference mean density by  $(1 + \Delta_0)$  in the power spectrum estimation also contributes to its responses, as shown below.

Let us derive analytically this separation of the growth and dilation effects in the power spectrum response functions. As in Sec. 2.3, we use  $\mathbf{p}$  to denote wavevectors in the local comoving coordinates, which is related to the global comoving wavevector  $\mathbf{k}$  by Eq. (2.39). At linear order, the density and tidal perturbations induce anisotropic responses in monopole and quadrupole. Therefore we define the total response functions  $R^E$ , including both growth and dilation effects, and the growth only response functions  $R^L$ , by

$$\begin{aligned} -\frac{\partial \ln P}{\partial \Delta_i^{(1)}} \Big|_{\mathbf{k}, \Delta=0} &\equiv R_0^E(k) + \mathcal{L}_2(\hat{k}_i) R_2^E(k), \\ -\frac{\partial \ln P_W}{\partial \Delta_i^{(1)}} \Big|_{\mathbf{p}, \Delta=0} &\equiv R_0^L(p) + \mathcal{L}_2(\hat{p}_i) R_2^L(p), \end{aligned} \quad (4.1)$$

where  $P_W$  is the power spectrum measured in local comoving space. The derivatives with respect to  $\Delta_i$  is taken holding the other two  $\Delta_j$ 's ( $j \neq i$ ) fixed, at  $\Delta = 0$  with  $\Delta$  being  $\Delta_0$  and  $\Delta_i$ 's. The function  $\mathcal{L}_2$  is the second order Legendre polynomial.

Our notation for power spectrum responses bear a resemblance to that of the halo biases. The linear halo bias can also be measured as responses of the halo abundance with respect to the long-wavelength density mode. One measures the Eulerian bias  $b^E$  or Lagrangian bias  $b^L$ , depending on whether the measurement is carried out in either global or local comoving space (see e.g. [4]), respectively. Therefore this ‘‘Lagrangian’’ superscript in  $R^L$  is not to be confused with *Lagrangian* perturbation theory in Sec. 2.2.

Because the variances should be conserved when transforming between Fourier-space volume elements,

$$P(\mathbf{k}; \Delta) d^3\mathbf{k} = (1 + \Delta_0)^2 P_W(\mathbf{p}; \Delta) d^3\mathbf{p}, \quad (4.2)$$

where the  $(1 + \Delta_0)^2$  factor on the right hand side is due to the change of reference density in  $P_W$ . Therefore for the dimensionless power spectra

$$k^3 P(\mathbf{k}; \Delta) = (1 + \Delta_0)^2 p^3 P_W(\mathbf{p}; \Delta). \quad (4.3)$$

Using Eq. (2.39) and the chain rule we can relate the total and growth responses in Eq. (4.1) by

$$\begin{aligned}
-\frac{\partial \ln k^3 P}{\partial \Delta_i^{(1)}} \Big|_{\mathbf{k}} &= 2 - \frac{\partial \ln p^3 P_W}{\partial \Delta_i^{(1)}} \Big|_{\mathbf{k}} = 2 - \frac{\partial \ln P_W}{\partial \Delta_i^{(1)}} \Big|_{\mathbf{p}} - \frac{\partial \ln p^3 P_W}{\partial p_j} \Big|_{\mathbf{\Delta}} \frac{\partial p_j}{\partial \Delta_i^{(1)}} \Big|_{\mathbf{k}} \\
&= 2 - \frac{\partial \ln P_W}{\partial \Delta_i^{(1)}} \Big|_{\mathbf{p}} - \hat{k}_i^2 \frac{d \ln k^3 P}{d \ln k}, \\
&= 2 - \frac{\partial \ln P_W}{\partial \Delta_i^{(1)}} \Big|_{\mathbf{p}} - \frac{1}{3} \frac{d \ln k^3 P}{d \ln k} - \mathcal{L}_2(\hat{k}_i) \frac{2}{3} \frac{d \ln k^3 P}{d \ln k}, \quad (4.4)
\end{aligned}$$

where  $\hat{k}_i = k_i/k$  and  $\mathbf{\Delta} = 0$  is assumed.

Therefore, the total (Eulerian) response and growth (Lagrangian) response are related through

$$\begin{aligned}
R_0^E &= 2 + R_0^L - \frac{1}{3} \frac{d \ln k^3 P}{d \ln k}, \\
R_2^E &= 0 + R_2^L - \frac{2}{3} \frac{d \ln k^3 P}{d \ln k}. \quad (4.5)
\end{aligned}$$

As explained in the beginning of this subsection, we have decomposed the total responses  $R^E$  into 3 contributions: the constant 2 due to the change of reference density, the growth responses  $R^L$ , and the dilation term proportional to the slope of the dimensionless power spectrum. Note the quadrupole response is not affected by the reference density, which is emphasized above with the 0.

In the linear regime  $P_W \propto D_W^2$  and we have calculated the modified growth factor  $D_W$  in Sec. 2.2. Rewriting Eq. (2.31) in Legendre polynomial,

$$D_W = D \left( 1 + \frac{13}{21} \Delta_0 - \frac{8}{21} \mathcal{L}_2(\hat{p}_i) \Delta_i^{(1)} \right), \quad (4.6)$$

so that the tree-level response functions are

$$\begin{aligned}
R_0^L &= \frac{26}{21}, & R_0^E &= \frac{68}{21} - \frac{1}{3} \frac{d \ln k^3 P}{d \ln k}; \\
R_2^L &= \frac{16}{21}, & R_2^E &= \frac{58}{21} - \frac{2}{3} \frac{d \ln k^3 P}{d \ln k}. \quad (4.7)
\end{aligned}$$

These results are consistent with the standard perturbation theory calculations, e.g. [13].

In the nonlinear regime, we need to numerically calibrate the response functions with simulations. We focus on the growth response because the other contributions in Eq. (4.5) are well understood, with the dilation term readily computable from the nonlinear power spectrum. A pure long tidal mode has only two degrees of freedom, as parametrized in Eq. (3.1) by  $\Delta_p$  and  $\Delta_e$ . It is straightforward to show that they modulate the power spectrum respectively by

$$\begin{aligned}
\delta P_W(\mathbf{p}; \Delta_p) &= -P(p) R_2^L(p) \Delta_p \mathcal{L}_2(\hat{p}_3), \\
\delta P_W(\mathbf{p}; \Delta_e) &= -P(p) R_2^L(p) \Delta_e [\mathcal{L}_2(\hat{p}_1) - \mathcal{L}_2(\hat{p}_2)]. \quad (4.8)
\end{aligned}$$

In practice, we measure  $R_2^L$  from those  $\Delta_p$ -type and  $\Delta_e$ -type of simulations

It is more straightforward to extract  $R_2^L$  from the  $\Delta_p$ -type simulations. Eq. (4.8) implies that the relevant changes in  $P_W$  lie in its quadrupole along the  $z$ -axis (denoted by  $\ell_p$  below),

$$P_W^{\ell_p=2}(p; \Delta_p) \equiv 5 \int \frac{d^2 \hat{\mathbf{p}}}{4\pi} P_W(\mathbf{p}; \Delta_p) \mathcal{L}_2(\hat{p}_3) = -P(p) R_2^L(p) \Delta_p, \quad (4.9)$$

due to the orthonormality of the Legendre polynomials and the fact that  $P(\mathbf{k})$  is isotropic. Therefore, the estimator for  $R_2^L(p)$  can be constructed as

$$R_2^L(p, z) = -\frac{P_W^{\ell_p=2}(p, z; \Delta_p = +\epsilon) - P_W^{\ell_p=2}(p, z; \Delta_p = -\epsilon)}{2\epsilon D(z) P(p, z)}. \quad (4.10)$$

Similarly, we can also estimate the growth response from the power spectrum quadrupoles along both  $x$  and  $y$  axes, from the  $\Delta_e$ -type simulations,

$$P_W^{\ell_e=2}(p; \Delta_e) \equiv 5 \int \frac{d^2 \hat{\mathbf{p}}}{4\pi} P_W(\mathbf{p}; \Delta_e) [\mathcal{L}_2(\hat{p}_1) - \mathcal{L}_2(\hat{p}_2)] = -P(p) R_2^L(p) \Delta_e, \quad (4.11)$$

where we have used the orthonormality of the Legendre polynomials and

$$\int \frac{d^2 \hat{\mathbf{p}}}{4\pi} \mathcal{L}_2(\hat{p}_1) \mathcal{L}_2(\hat{p}_2) = -\frac{1}{10}. \quad (4.12)$$

Thus, we can estimate  $R_2^L(p)$  by

$$R_2^L(p, z) = -\frac{P_W^{\ell_e=2}(p, z; \Delta_e = +\epsilon) - P_W^{\ell_e=2}(p, z; \Delta_e = -\epsilon)}{2\epsilon D(z) P(p)}. \quad (4.13)$$

#### 4.1.1 Responses at high redshifts from 2LPT

At high redshifts 2LPT works accurately with more modes in the linear regime. Using results derived in Sec. 2.2, we have modified the initial condition generator to incorporate the leading order impact of the long modes to the 2LPT. This allows us to measure the power spectrum responses reliably at high redshifts. For this purpose, we have generated 8 pairs of 2LPT realizations with  $\Delta_p$ -type tides and  $1024^3$  particles in  $100 \text{ Mpc}/h$  boxes at  $z = 49, 15, 10$ , and  $7$ .

We first compare the isotropic response  $R_0^L$  measured from our 2LPT to that from the usual separate universe simulations, in order to find out the scale above which our 2LPT responses converge. Fig. 9 in App. D shows the results of this convergence test. The isotropic 2LPT responses are accurate to within 5% of the separate universe results, for  $k \leq 9 \text{ h/Mpc}$  at  $z = 15$ ,  $k \leq 4 \text{ h/Mpc}$  at  $z = 10$ , and  $k \leq 2 \text{ h/Mpc}$  at  $z = 7$ . These scales are shown as vertical dotted lines in Fig. 1.

We measure the 2LPT response  $R_2^L$  at each redshift, and show the results in Fig. 1. Note that we have scaled the vertical axis for easy comparison with previous studies,  $3R_2^L(p)/2 = G(k)$  used in Refs. [9–11]. It is clear that at these high redshifts  $R_2^L(p)$  grows more than the prediction of tree-level perturbation theory on small scales for  $k \geq 2 \text{ h/Mpc}$ . While the overall trend is in agreement with the results of Ref. [11], our responses have quantitatively less enhancement than that in Ref. [11], even after taking into account the possible error of 2LPT. This may be attributed to the difference on implementations details, e.g. generating initial condition at different orders, and needs the further examination.

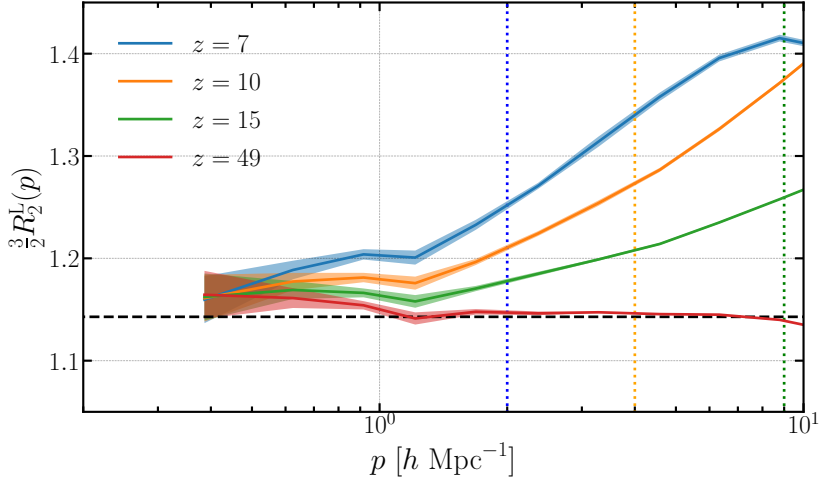


**Figure 1:** Power spectrum growth response function to the large-scale tidal fields,  $R_2^L$ , measured at high redshifts from 2LPT realizations. The shaded region shows the  $1\sigma$  error. At  $z = 49$ , the response agrees well with the linear perturbation theory prediction on all scales, which is shown by the horizontal dashed line, while at later times the responses are enhanced on small scales. Vertical dotted lines mark for each redshift the convergence scale, above which isotropic 2LPT responses  $R_0^L$  converge to within 5% of the validation separate universe simulations. Though of similar trend, our results show quantitatively less enhancement than that in Ref. [11], even after taking into account the possible error of 2LPT.

#### 4.1.2 Responses at low redshifts from $N$ -body

Although Refs. [9, 10] already investigated the linear tidal response of matter power spectrum from their simulations, we also measured the Lagrangian response  $R_2^L(p)$  at low redshift from our  $N$ -body simulations to check the validity of our numerical implementation. In this subsection we show results from 1 Gpc/ $h$  simulations to cover both linear and nonlinear regimes.

First, since we ran two different types of tidal simulations ( $\Delta_p$ - and  $\Delta_e$ -type), we tested whether simulations with different type of tides give converging results. In Fig. 2a we present  $R_2^L(p)$  from both  $\Delta_p$ -type simulations (Eq. (4.10)) and  $\Delta_e$ -type simulations (Eq. (4.13)). Both results agree well up to  $k = 10 h/\text{Mpc}$ . Therefore we combine  $\Delta_e$ - and  $\Delta_p$ -type simulations to estimate  $R_2^L(p)$  in the results below.

Fig. 2b shows  $R_2^L(p)$  for several redshifts;  $z = 3, 2, 1, 0.5$ , and 0. At these low redshifts,  $R_2^L(p)$  decreases over all scales as the redshift decreases. This is likely because strong nonlinearity tends to erase the memory of large-scale tidal field gradually. Although these features are in general consistent with previous studies, quantitatively there is a small difference. For instance, at  $z = 3$  tidal response from our simulations takes a maximum  $3R_2^L/2 \sim 1.5$  while in Ref. [11] the maximum at  $z = 3$  is less than 1.5. In addition, Ref. [9] reports the different behaviour of  $R_2^L$  at  $z = 2$  to ours. These disagreements may arise from the halo sample variance in the nonlinear regime, which is also seen in the separate universe simulations (e.g. Ref. [1]) or the difference in details of the numerical implementations and require further studies.



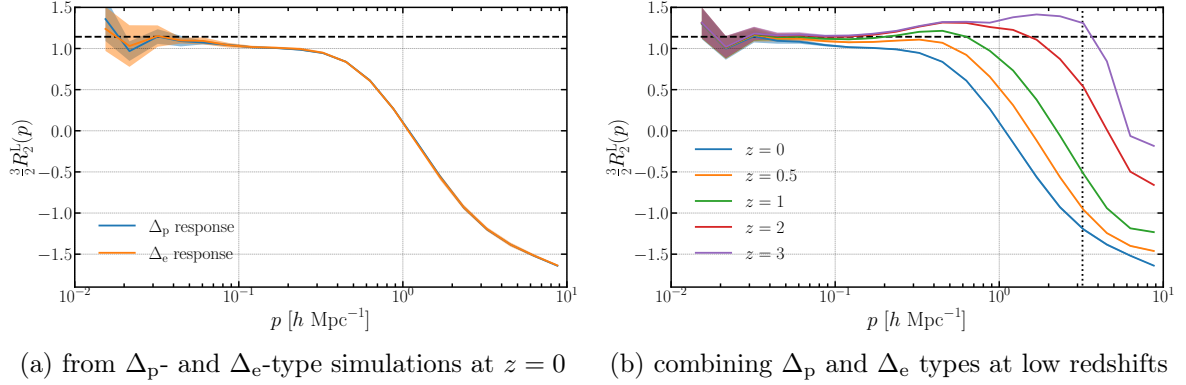


**Figure 2:** Power spectrum responses as in the previous figure, measured at low redshifts from  $N$ -body simulations with  $L = 1 \text{ Gpc}/h$ . The shaded region shows the  $1\sigma$  error. The horizontal dashed line is the tree-level perturbation theory prediction. The vertical dotted line on the right panel depicts the particle Nyquist wavenumber for  $L = 1 \text{ Gpc}/h$  simulations.

## 4.2 Halo shape response

It is well known that tidal fields affect the intrinsic alignment of galaxy shapes. Likewise, halo shapes also respond to the large-scale tidal modes, with the sensitivity captured by the shape bias. This is analogous to the halo bias which is the response of the halo abundance to the large-scale density mode. In this section, we present measurements of the shape bias using our tidal simulations. We show its universal behavior as a function of the linear bias, and its dependence on properties beyond mass, an effect that we call the shape assembly bias.

We identify dark matter halos from our simulations with **AHF** [36]. It uses adaptively refined meshes to find local density peaks as centers of prospective halos. It then defines the halos as spherical overdensity (SO) regions  $\Delta_h$  times denser than the mean matter density  $\bar{\rho}_m$ . We choose  $\Delta_h = 200$ , and disable the gravitational unbinding procedure to find the host halos with more than 400 particles. While we need to identify SO halos in the global comoving coordinates, **AHF** by default uses the simulation coordinates that is local comoving, so that halos are not identified as the spherical overdensity in the global ones. Therefore, we modify the **AHF** code to use the Euclidean metric for the halo identification in the global coordinates.

Given an SO halo, we define its quadrupole shape in two ways, the inertia tensor and the reduced inertia tensor. The former is defined as

$$I_{ij} \equiv \sum_{i=1}^{N_p} m_p x_i x_j, \quad (4.14)$$

summing over all  $N_p$  particle of the halo.  $m_p$  is the particle mass and  $x_i$  is  $i$ -th components of the particle location with respect to the halo center. In the literature  $I_{ij}$  is sometimes normalized by the halo mass, which however does not affect our response measurement presented below.

The reduced inertia tensor is defined similarly but with additional radius weighting

$$J_{ij} \equiv \sum_{i=1}^{N_p} m_p \frac{x_i x_j}{x^2}, \quad (4.15)$$

where  $x$  is the distance of a particle to the halo center. This definition uses a dimensionless ratio and therefore weight each mass equally only by angular position regardless of radial distance  $x$ . Compared to Eq. (4.14),  $J_{ij}$  upweights the inner masses and thus should be more strongly correlated with properties of galaxies which reside in the halo.<sup>4</sup> Therefore, in the following main text, we use  $J_{ij}$  to estimate halo shapes. The results from  $I_{ij}$  are summarized in App. E. Ref. [40] also presented comparisons of  $I_{ij}$  and  $J_{ij}$  in the context of intrinsic alignments of galaxies (see their Appendix B).

According to the linear alignment model, at the leading order the halo shapes responds to the external tidal field as

$$J_{ij} = J_0 \left[ \frac{1}{3} \delta_{ij}^K + b_K K_{ij} \right], \quad (4.16)$$

where  $J_0$  is the trace component of the shape tensor:  $J_0 = \text{Tr}[J_{ij}]$ ,  $K_{ij}$  is the DC tidal field:  $K_{ij} = (\partial_i \partial_j / \partial^2 - \delta_{ij}^K / 3) \delta$  and  $b_K$  is the dimensionless linear shape bias parameter, which is related to the conventionally used linear alignment coefficient  $C_1$  through  $b_K = -a^3 C_1 \bar{\rho}(a) / D(a)$ . The shape bias  $b_K$  represents the strength of the response or alignment and thus an analogous parameter to the linear bias  $b_1$ , which describes the response of the number density of halos to the spherically symmetric long-wavelength perturbation:  $\delta_h = b_1 \delta$ .

Following the decomposition of the traceless components of the background tide into  $\Delta_p$  and  $\Delta_e$ , it is convenient to define the following two quantities

$$J_p \equiv J_{33} - \frac{J_{11} + J_{22}}{2}, \quad (4.17)$$

$$J_e \equiv \frac{J_{11} - J_{22}}{2}. \quad (4.18)$$

Then, Eq. (4.16) implies

$$b_K(M, z) = - \frac{J_p(M, z; \Delta_p = +\epsilon) - J_p(M, z; \Delta_p = -\epsilon)}{2\epsilon D(z) J_0(M, z)}, \quad (4.19)$$

$$b_K(M, z) = - \frac{J_e(M, z; \Delta_e = +\epsilon) - J_e(M, z; \Delta_e = -\epsilon)}{2\epsilon D(z) J_0(M, z)}, \quad (4.20)$$

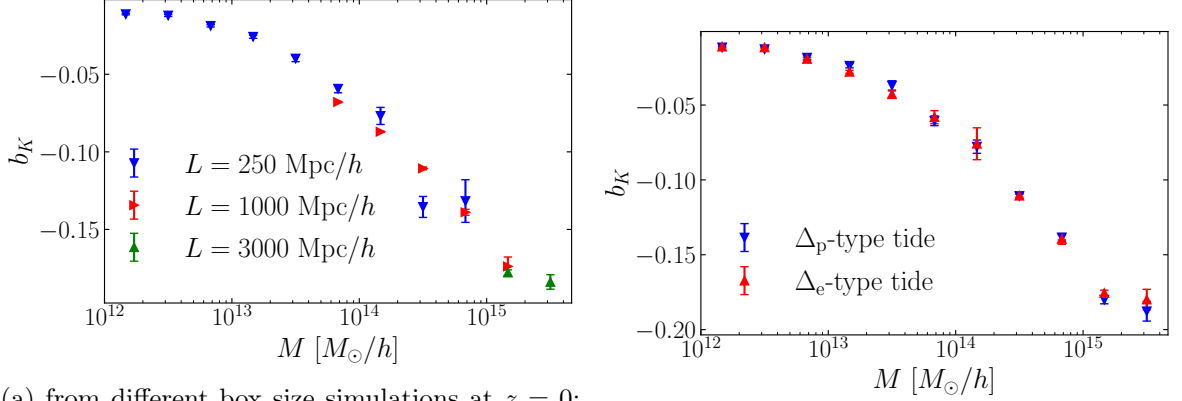
for  $\Delta_p$ -type and  $\Delta_e$ -type simulations, respectively. Having these relations, we can estimate  $b_K$  from our tidal simulations by measuring the averaged trace of the shape tensor,  $J_0$ , and the averaged traceless components  $J_p$  and  $J_e$  from fiducial,  $\Delta_p$ -type, and  $\Delta_e$ -type simulations respectively.

Note that the linear shape bias  $b_K$  measured in this way should be regarded as the Lagrangian shape bias since we do not take into account the volume distortion due to the background strain. For linear shape bias, however, there is no difference between the Lagrangian shape bias  $b_K^L$  and the Eulerian one  $b_K^E$  unlike the number density bias where the Lagrangian linear bias  $b_1^L$  is related to the Eulerian one  $b_1^E$  through  $b_1^E = b_1^L + 1$ . This is because the pure tidal field does not induce the volume distortion at linear order of the tide and can be explicitly shown by considering the conservation laws:  $J_{ij}^E(\mathbf{x}) d^3 \mathbf{x} = J_{ij}^L(\mathbf{q}) d^3 \mathbf{q}$  and  $(1 + \delta^E(\mathbf{x})) d^3 \mathbf{x} = d^3 \mathbf{q}$ <sup>5</sup>. Thus, in this paper we do not distinguish  $b_K^L$  from  $b_K^E$  and the linear shape bias is just written as  $b_K$ .

<sup>4</sup>See, e.g., Refs. [37–39] for the detection of large misalignments ( $\sim 30$  deg) between the major axes of central galaxies and their host halos when  $I_{ij}$  is used to define halo shapes.

<sup>5</sup>For the second order shape bias, the Lagrangian shape bias is no longer identical to the Eulerian one. See the discussion in [41]

#### 4.2.1 Convergence on the resolution and external tides



(a) from different box size simulations at  $z = 0$ :

$L = 250$  Mpc/h (blue),  $L = 1$  Gpc/h (red), and  $L = 3$  Gpc/h (green),.

(b) from different tides,  $\Delta_p$ -type (red) and  $\Delta_e$ -type (blue), at  $z = 0$ .

**Figure 3:** Linear alignment coefficient,  $b_K$ , for the reduced inertial tensor,  $J_{ij}$

Before showing the redshift- and environment-dependence of  $b_K$ , here we discuss the convergence of measured  $b_K$  for different resolutions and different kinds of tides.

Figure 3a shows  $b_K$  from different boxsize simulations, meaning the different resolutions since we fix the number of particles. The results are in agreement with each other over all mass range except for 6th-8th mass-bin where the result from 250 Mpc/h and 1 Gpc/h simulations have a small difference. For 6th and 7th mass-bin, these differences can be attributed to not enough number of particles in the inner regime of halos in 1 Gpc/h simulation to determine halo shapes, given that the results from  $I_{ij}$  are converged at these mass-bins (see Fig. 11a in App. E). On the other hand, at 8th mass-bin  $b_K$  from 250 Mpc/h simulations are not in agreement with that from 1 Gpc/h for both  $J_{ij}$  and  $I_{ij}$  results. This could happen due to the small number of halos at this mass-bin in 250 Mpc/h simulations. Considering these results, in the following we use 250 Mpc/h, 1 Gpc/h, and 3 Gpc/h simulations for 1st-7th, 8th-9th, and 10th-11th mass-bin, respectively.

In Fig. 3b we show the results from different kinds of tides, namely  $\Delta_p$ -type and  $\Delta_e$ -type tides. They are in good agreement with each other, which implies that the validity of the linear alignment model is irrelevant to the substructure of the cosmic web such as knots, filaments, or pancakes. Because the results from the two different tides are converged over all mass range, in the following we combine two kinds of simulations to estimate  $b_K$ .

#### 4.2.2 Redshift-dependence: the relation between $b_K$ and $b_1^E$

Here we discuss the redshift-dependence of the linear alignment coefficient and show that there seems an universal relation between  $b_K$  and  $b_1$ .

Fig. 4 shows the linear alignment coefficient,  $b_K$ , for different redshifts. It is clear that the absolute value of  $b_K$  is greater at more massive halos and at higher redshift. This means that more massive halos align stronger than less massive ones and the strength of the alignment becomes larger as redshift increases for all mass range. These trends are supposed to originate from the fact that the alignment of halo shape is also affected by the surrounding matter distribution of each halos; less massive halos are susceptible to their surroundings and as time evolves the impact of their surroundings becomes greater.

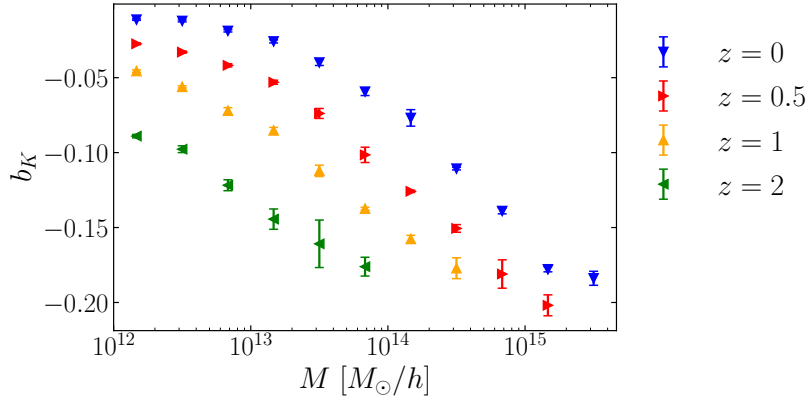


**Figure 4:** Linear alignment coefficient,  $b_K$ , for the reduced inertial tensor,  $J_{ij}$ , at various redshifts:  $z = 0$  (blue),  $z = 0.5$  (red),  $z = 1$  (orange),  $z = 2$  (green). Here we combine the results from difference boxsize and difference tides simulations.

These trends are similar to the linear bias  $b_1$  so it is interesting to explore the relation between  $b_K$  and  $b_1$ . In Fig. 5 we plot  $b_K$  as a function of the Eulerian linear bias  $b_1^E$  for various redshifts.  $b_1^E$  is estimated from the Lagrangian linear bias  $b_1^L$ , which is directly measured as the response of the halo number in our  $\Delta_0$ -type simulations (see also App. D), using  $b_1^E = b_1^L + 1$ . We find the relation between  $b_K$  and  $b_1^E$  shows an universal behaviour over the range  $z = 0 \sim 2$ . This universal relation is also found when using  $I_{ij}$  (see App. E) and thus is not relevant to how to measure the halo shapes. This strongly suggests that  $b_K$  is also uniquely determined by some quantity depending mass as  $b_1^E$  does by the variance of the dark matter density field. Since our simulations enable both  $b_K$  and  $b_1$  to be measured very accurately, here we provide the fitting formula in the form of  $b_K(b_1^E)$  for convenience. We combine results from all redshifts and obtain a fitting formula of the  $b_K$ - $b_1$  relation using a very simple rational function:

$$b_K = \frac{0.06461 - 0.09322b_1^E}{1 + 0.3073b_1^E} \quad (4.21)$$

The fitting curve is shown as dashed line in Fig. 5.

#### 4.2.3 Secondary halo shape responses

Studies of the halo assembly bias show that the halo bias depends on properties other than the mass. Likewise, it is natural that the halo shape response also possesses rich dependences beyond the halo mass. Here we study dependences of  $b_K$  on the halo concentration and the eccentricity of inertial tensor of halos.

We use the AHF halo finder to measure the halo concentration parameter  $c$ . Instead of fitting a NFW halo profile to each halo, AHF measures the ratio  $v_{\max}/v_{200}$ .  $v_{\max}$  is the maximum circular velocity,  $v_{\max} \equiv \max \sqrt{GM(< R)/R}$ , and  $v_{200}$  is the circular velocity at virial radius  $v_{200} \equiv \sqrt{GM_{200}/R_{200}}$ . Assuming a NFW halo profile,  $v_{\max}/v_{200}$  is related to  $c$  as given by [42], and thus is used in AHF to determine the concentration.

At each redshift and mass-bin we divided halo samples into those with greater than the median of the concentration and those with smaller concentration. Then we measured  $b_K$  from each group. The results are shown in Fig. 6. For all redshifts halos with lower concentration

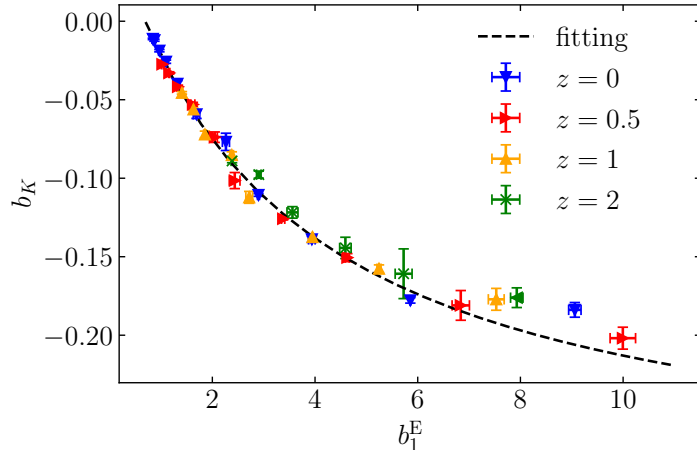


**Figure 5:** Linear alignment coefficient,  $b_K$ , as a function of the Eulerian linear bias,  $b_1^E$ , combining all redshift and mass information. The dashed curve is the fitting given in Eq. (4.21).

tend to have a large amplitude of  $|b_K|$  at high mass, while the difference is likely to become small at low mass. Since halos with the high concentration are expected to be formed from highly curved peaks [43], the process of collapse into halo is not expected to be much affected by large-scale tidal field. Further, since they were formed earlier they tend to lose their memory on large-scale tidal field through interacting with the local surroundings for a long time.

Next we discuss a dependence of the axis-ratio of halo shapes on  $b_K$ . We introduce the axis-ratio as the ratio of the major axis to the minor axis of the shape tensor:  $q \equiv J_3/J_1$  where  $J_1$ ,  $J_2$ , and  $J_3$  are the eigenvalues of  $J_{ij}$  satisfying  $J_1 \geq J_2 \geq J_3$ . As is done in the concentration, we divided halo samples into two groups: those above the median of the axis-ratio and those below the median, and then measured  $b_K$  from each group. Fig. 7 presents the results. For all redshifts and mass bins  $|b_K|$  from lower  $q$  samples is greater than higher  $q$  samples, which means that halos with rounder shapes do not respond to the large-scale tidal field as strongly as halos with greater ellipticity. This implies that distortion of halo shapes is indeed accelerated by the large-scale tidal field. The same trend is found for a study of intrinsic alignments in Ref. [39]: more elongated halos are more tightly aligned with the surrounding matter distribution. Thus, the existence of the DC mode would not only bias measurements of the cosmic shear power spectrum in weak lensing surveys but also affect the cosmological application of intrinsic alignment itself.

## 5 Discussion

In this paper, we have implemented mean (DC) tidal and density fluctuations into cosmological  $N$ -body simulations by absorbing them in effective anisotropic background expansion. We have improved upon previous works [8–11] on generating initial conditions for the tidal simulations, with full second order Lagrangian dynamics properly solved in general anisotropic background.

The 2LPT in anisotropic background can be used to investigate the linear tidal response of the matter power spectrum,  $R_2^L$ , on quasi-nonlinear scales. Since in simulations  $R_2^L$  at high redshifts suffer from various numerical artifacts [9], it is of particular interest to measure  $R_2^L$  on small scales at high redshifts from the 2LPT. We have found  $R_2^L$  is enhanced upon the

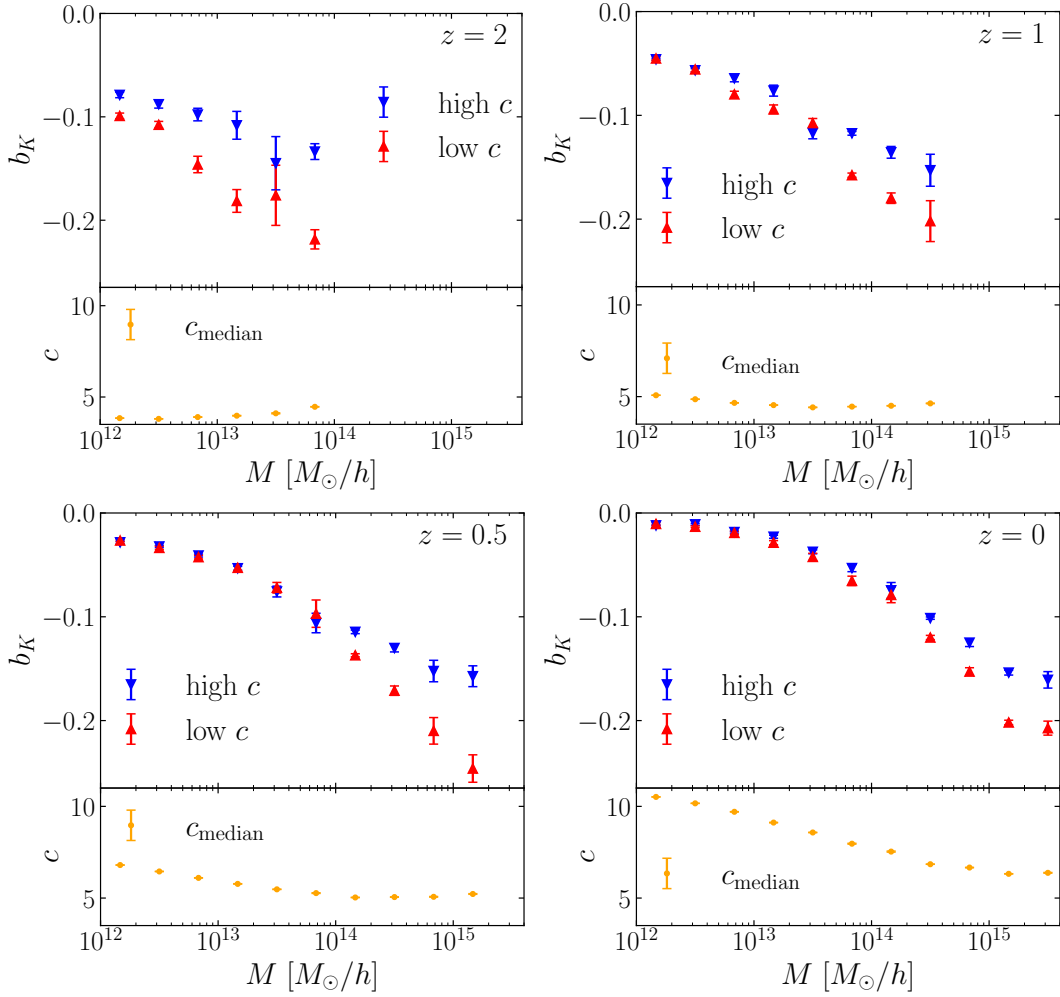


**Figure 6:** *Upper panel:* The halo concentration dependence of the linear alignment coefficient,  $b_K$ , at various redshifts and masses:  $b_K$  from high concentration (blue) and low concentration (red). *Left panel:* The median concentration on which we divided halo samples.

tree-level perturbation theory prediction at  $z = 7 \sim 15$ . Our 2LPT results should be more robust since they are not affected by high-redshift numerical artifacts that affect  $N$ -body simulations. Though our findings are qualitatively consistent with the result of Ref. [11], our enhancement is quantitatively weaker than that in Ref. [11].

We have also investigated the effect of large-scale tidal field on three-dimensional halo shapes using our simulations. The linear alignment model predicts that the halo shape responds to the large-scale tidal field and thus linearly related with each other:  $J_{ij} = b_K K_{ij}$ . Our tidal simulations allow us to directly test this relation and measure the proportional coefficient  $b_K$  accurately. We have found that the dependence of  $b_K$  on redshifts and halo mass is similar to that of the linear halo bias  $b_1^E$ ; i.e., at the same halo mass  $|b_K|$  is getting smaller as redshift decrease and more massive halos have greater  $|b_K|$ . Furthermore, we have noticed that the relation between  $b_K$  and  $b_1^E$  shows the universal behaviour over wide range of redshifts and masses;  $z = 0 \sim 2$  and  $M_h = 10^{12} \sim 10^{15} M_\odot/h$ . This implies that we can construct an analytical, physical model that can properly describe the mass- and redshift-dependence

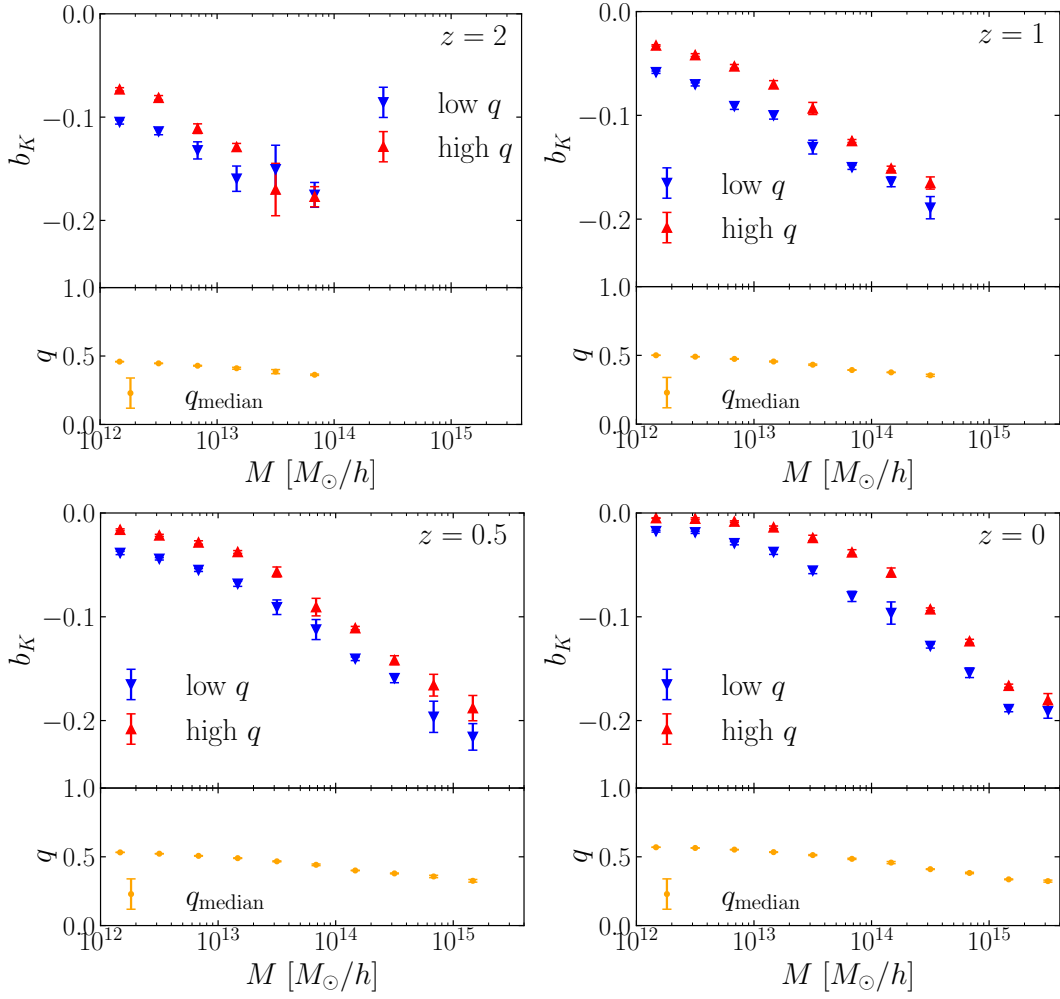


**Figure 7:** *Upper panel:* The axis-ratio ( $q = J_3/J_1$  with  $J_1 \geq J_3$ ) dependence of the linear alignment coefficient,  $b_K$ , at various redshifts and masses:  $b_K$  from high  $q$  (low ellipticity, blue) and low  $q$  (high ellipticity, red). *Left panel:* The median axis-ratio on which we divided halo samples.

of  $b_K$  as done for the linear bias using the peak theory and excursion set approach. This kind of the theoretical prediction on  $b_K$  is quite useful especially when treating the intrinsic alignments as the signal. In particular, such a model is of crucial importance for exploring the angular-dependent (quadrupolar) primordial non-Gaussianity (PNG) from observations of the intrinsic alignments. It is pointed out that the intrinsic alignments can uniquely probe the quadrupolar PNG in Refs. [23, 24]. However, since the bias induced by the quadrupolar PNG on halo or galaxy shapes is completely degenerated with the quadrupolar PNG signal, the lack of such a model makes it impossible to extract the information on the quadrupolar PNG from measurements of the intrinsic alignments. Therefore to develop a theory for the linear alignment coefficient  $b_K$ , analogous to the linear bias  $b_1$  case, is an urgent issue and worth exploring in future works.

In addition, we have measured for the first time the secondary dependence of  $b_K$  on halo properties other than the mass; it also depends on the halo concentration and axis-ratio. This

can be seen as the shape “assembly bias” as in the case of the number density bias <sup>6</sup>. These findings will help to understand how halo shapes are determined in the hierarchical structure formation.

## Acknowledgments

KA acknowledge support from JSPS Research Fellowship for Young Scientists and JSPS KAKENHI Grant Numbers JP19J12254 and JP19H00677. YL acknowledge support from Fellowships at Simons Foundation, the Kavli IPMU established by World Premier International Research Center Initiative (WPI) of the MEXT Japan, and at the Berkeley Center for Cosmological Physics. TO acknowledges support from the Ministry of Science and Technology of Taiwan under Grants No. MOST 109- 2112-M-001-027- and the Career Development Award, Academia Sinica (AS-CDA-108-M02) for the period of 2019 to 2023.

## A Solving DC density mode at second order

At second order, Eq. (2.12) gives

$$\ddot{\Delta}_i^{(2)} + 2H\dot{\Delta}_i^{(2)} = 4\pi G\bar{\rho}_m \left( \Delta_i^{(1)2} - \frac{1}{3}\Delta_0^{(2)} \right). \quad (\text{A.1})$$

Also expand Eq. (2.9) at second order and use Eq. (2.14) to derive

$$\Delta_0^{(2)} = - \sum_i \Delta_i^{(2)} + \sum_{i<j} \Delta_i^{(1)} \Delta_j^{(1)} + \sum_i \Delta_i^{(1)2} = - \sum_i \Delta_i^{(2)} + \frac{1}{2}\Delta_0^{(1)2} + \frac{1}{2} \sum_i \Delta_i^{(1)2}. \quad (\text{A.2})$$

Sum over  $i$  of the first equation and plug in the second one, one can show that at matter dominated era

$$\sum_i \Delta_i^{(2)} = \frac{3}{14} \sum_i \Delta_i^{(1)2} - \frac{3}{14} \Delta_0^{(1)2}. \quad (\text{A.3})$$

Thus

$$\Delta_0^{(2)} = \frac{5}{7} \Delta_0^{(1)2} + \frac{2}{7} \sum_i \Delta_i^{(1)2} = \frac{17}{21} \Delta_0^{(1)2} + \frac{2}{7} \sum_i \tau_i^2, \quad (\text{A.4})$$

where the last equality follows from Eq. (2.13).

## B Second order Lagrangian perturbation theory in an anisotropic background

For 2LPT, the Jacobian determinant and matrix inverse in the master equation Eq. (2.19) can be expanded as

$$\left| \frac{\partial \mathbf{x}}{\partial \mathbf{q}} \right| \simeq 1 + \sum_i \Psi_{i,i}^{(1)} + \sum_i \Psi_{i,i}^{(2)} + \frac{1}{2} \left[ \sum_i \left( \Psi_{i,i}^{(1)} \right)^2 - \sum_{ij} \Psi_{i,j}^{(1)} \Psi_{j,i}^{(1)} \right] \quad (\text{B.1})$$

$$[\delta_{ij} + \Psi_{i,j}]^{-1} \simeq \delta_{ij} - \Psi_{i,j}^{(1)}, \quad (\text{B.2})$$

---

<sup>6</sup>Refs. [44, 45] discuss the impact of the intrinsic alignment or galaxy shape on the density tracer as the assembly bias. This should be distinguished with ours that is the assembly bias *of* the intrinsic alignment.



leading to the second-order equation

$$\begin{aligned}
& \sum_i \ddot{\Psi}_{i,i}^{(2)} + 2 \sum_i H_i \dot{\Psi}_{i,i}^{(2)} - \frac{3}{2} H^2 \Omega_m(a) (1 + \Delta_0) \sum_i \Psi_{i,i}^{(2)} \\
&= - \sum_i \Psi_{i,i}^{(1)} \sum_j \left[ \ddot{\Psi}_{j,j}^{(1)} + 2H_j \dot{\Psi}_{j,j}^{(1)} \right] + \sum_{ij} \Psi_{i,j}^{(1)} \left[ \ddot{\Psi}_{i,j}^{(1)} + 2H_i \dot{\Psi}_{i,j}^{(1)} \right] \\
&+ \frac{3}{2} H^2 \Omega_m(a) (1 + \Delta_0) \left[ \frac{1}{2} \sum_i \left( \Psi_{i,i}^{(1)} \right)^2 - \frac{1}{2} \sum_{ij} \Psi_{i,j}^{(1)} \Psi_{j,i}^{(1)} \right]. \quad (\text{B.3})
\end{aligned}$$

Similar to the linear order, we introduce the second order displacement potential through  $\Psi_i^{(2)} = \partial \psi_W^{(2)} / \partial q_i \equiv \psi_{W,i}^{(2)}$ . In the absence of the long modes, the equation for  $\psi^{(2)}$  reduces to

$$\sum_i \ddot{\psi}_{,ii}^{(2)} + 2H \sum_i \dot{\psi}_{,ii}^{(2)} - \frac{3}{2} H^2 \Omega_m(a) \sum_i \psi_{,ii}^{(2)} = - \frac{3}{2} H^2 \Omega_m(a) \left[ \frac{1}{2} \left( \sum_i \psi_{,ii}^{(1)} \right)^2 - \frac{1}{2} \sum_{ij} \psi_{,ij}^{(1)} \psi_{,ji}^{(1)} \right], \quad (\text{B.4})$$

where we used the linear equation Eq. (2.23). In this usual case, we denote the time-dependent part of  $\psi^{(2)}$  as  $D^{(2)}(t)$ , which obeys

$$\ddot{D}^{(2)} + 2H \dot{D}^{(2)} - \frac{3}{2} H^2 \Omega_m(a) D^{(2)} = - \frac{3}{2} H^2 \Omega_m D^{(1)2}. \quad (\text{B.5})$$

In the matter-domination, we have  $D^{(2)} = 3D^{(1)2}/7$ . The correction induced by the long modes, which is expressed by  $\epsilon^{(2)}(t, \mathbf{q}) \equiv \psi_W^{(2)}(t, \mathbf{q}) - \psi(t, \mathbf{q})$ , follows

$$\begin{aligned}
& \sum_i \ddot{\epsilon}_{,ii}^{(2)} + 2H \sum_i \dot{\epsilon}_{,ii}^{(2)} - \frac{3}{2} H^2 \Omega_m(a) \sum_i \epsilon_{,ii}^{(2)} = \\
& - 2 \sum_i \dot{\psi}_{,ii}^{(2)} \Delta_i + 2 \sum_{ij} \dot{\Delta}_i \dot{\psi}_{,ij}^{(1)} \psi_{,ji}^{(1)} - \frac{3}{2} H^2 \Omega_m(a) \sum_j \epsilon_{,jj}^{(1)} \sum_i \psi_{,ii}^{(1)} \\
& + \sum_{ij} \psi_{,ij}^{(1)} \left[ \ddot{\epsilon}_{,ij}^{(1)} + 2H \dot{\epsilon}_{,ij}^{(1)} \right] \\
& + \frac{3}{2} H^2 \Omega_m(a) \Delta_0 \left[ \sum_i \psi_{,ii}^{(2)} - \frac{1}{2} \sum_i \left( \psi_{,ii}^{(1)} \right)^2 - \frac{1}{2} \sum_{ij} \psi_{,ij}^{(1)} \psi_{,ji}^{(1)} \right], \quad (\text{B.6})
\end{aligned}$$

where we have neglected  $\mathcal{O}(\Delta_i^2)$  terms. Notice that  $\epsilon^{(1)}$  is  $\mathcal{O}(\Delta_i)$ . For the matter dominated era, the solution for Eq. (B.6) is given by

$$\begin{aligned}
\sum_i \epsilon_{,ii}^{(2)}(t, \mathbf{q}) &= \frac{1}{4} \sum_i \left[ -\frac{16}{9} \psi_{,ii}^{(2)}(t, \mathbf{q}) + \frac{8}{9} \sum_j \psi_{,ij}^{(1)}(t, \mathbf{q}) \psi_{,ji}^{(1)}(t, \mathbf{q}) \right] \Delta_i \\
&+ \frac{1}{6} \left[ \sum_i \psi_{,ii}^{(2)} - \frac{1}{2} \sum_i \left( \psi_{,ii}^{(1)} \right)^2 - \frac{1}{2} \sum_{ij} \psi_{,ij}^{(1)} \psi_{,ji}^{(1)} \right] \Delta_0 \\
&+ \frac{1}{4} \left[ -\frac{2}{3} \sum_i \psi_{,ii}^{(1)}(t, \mathbf{q}) \sum_j \epsilon_{,jj}^{(1)}(t, \mathbf{q}) + \frac{20}{9} \sum_{ij} \psi_{,ij}^{(1)}(t, \mathbf{q}) \epsilon_{,ij}^{(1)}(t, \mathbf{q}) \right]. \quad (\text{B.7})
\end{aligned}$$

Although the modified second order growth factor,  $D_W^{(2)}$ , due to the long modes can be identified as  $D_W^{(2)}(t, \mathbf{p}) = D^{(2)}(1 + \Delta_0/6 - 4\hat{p}_i^2 \Delta_i/9)$ , the local gravitational tides cannot be neglected at second order.

## C Force computation

In this appendix, we review how to evaluate the tree force, especially the real-space counterparts of the PM force.  $\phi^{\text{PM}}(\mathbf{x})$  satisfies

$$\sum_i (1 + \Delta_i)^{-2} \frac{\partial^2}{\partial x_i^2} \phi^{\text{PM}}(\mathbf{x}) = -4\pi G \bar{\rho}_m a^2 (1 + \Delta_0) \int d^3 \mathbf{x}' \delta(\mathbf{x}') \cdot \left[ \frac{1}{8\pi \sqrt{\pi} x_s^3} \exp\left(-\frac{|\mathbf{x} - \mathbf{x}'|^2}{4x_s^2}\right) \right], \quad (\text{C.1})$$

where the function inside the last bracket corresponds to the Fourier transform of  $\exp(-p^2 x_s^2)$ , which is the Gaussian smoothing kernel used in Eq. (2.38) to split force. The PM potential is related to the tree potential as  $\phi^{\text{PM}} = \phi - \phi^{\text{T}}$  and the solution for the PM potential is found to be

$$\phi^{\text{PM}}(\mathbf{x}) = -\frac{Gm}{2a\sqrt{\pi}x_s} \int_0^\infty \frac{\exp\left[-\frac{1}{4x_s^2} \left( \frac{(1+\Delta_1)^2 x^2}{(1+\Delta_1)^2 + \lambda} + \frac{(1+\Delta_2)^2 y^2}{(1+\Delta_2)^2 + \lambda} + \frac{(1+\Delta_3)^2 z^2}{(1+\Delta_3)^2 + \lambda} \right)\right]}{\sqrt{((1+\Delta_1)^2 + \lambda)((1+\Delta_2)^2 + \lambda)((1+\Delta_3)^2 + \lambda)}} d\lambda, \quad (\text{C.2})$$

where we used  $\bar{\rho}_m(1 + \Delta_0)[1 + \delta(\mathbf{x})] = m(1 + \Delta_0)/a^3 \cdot \sum_n \delta^{\text{D}}(\mathbf{x} - \mathbf{x}_n)$ . Although (C.2) has no closed analytic form, we can approximate this potential by Taylor expansion in  $\Delta_i$ <sup>7</sup>. Using the following identity

$$I_k(r) \equiv \int_0^\infty \frac{\exp\left[-\frac{1}{4x_s^2} \frac{r^2}{a^2(1+\lambda)}\right]}{\sqrt{(1+\lambda)^k}} d\lambda = \left(\frac{r}{2ax_s}\right)^{2-k} \gamma\left(\frac{k-2}{2}, \frac{r^2}{4a^2x_s^2}\right) \quad (\text{C.3})$$

where  $\gamma$  is the lower incomplete gamma function. We can express the approximated  $\phi^{\text{PM}}(\mathbf{x})$  up to the second order of  $\Delta_i$  as

$$\begin{aligned} \phi^{\text{PM}}(\mathbf{r}) = & -\frac{Gm}{2a\sqrt{\pi}x_s} \left[ I_3(r) + \sum_i \left( -I_5(r) + \frac{r_i^2}{2a^2x_s^2} I_7(r) \right) \Delta_i \right. \\ & + \frac{1}{2} \sum_i \left( -I_5(r) + \left( 3 + \frac{r_i^2}{2a^2x_s^2} \right) I_7(r) - \frac{3r_i^2}{a^2x_s^2} I_9(r) + \frac{r_i^4}{4a^4x_s^4} I_{11}(r) \right) \Delta_i^2 \\ & \left. + \frac{1}{2} \sum_{i \neq j} \left( I_7(r) - \frac{r_i^2 + r_j^2}{2a^2x_s^2} I_9(r) + \frac{r_i^2 r_j^2}{4a^4x_s^4} I_{11}(r) \right) \Delta_i \Delta_j \right] + \mathcal{O}(\Delta_i^3). \end{aligned} \quad (\text{C.4})$$

In order to derive the force from this potential, we must be careful that the derivative should be taken with respect to the local comoving coordinate  $\mathbf{x}$ , not to  $\mathbf{r}$ . Thus, the force from the PM potential is computed as

$$\frac{\partial \phi^{\text{PM}}}{\partial x^k} = a(1 + \Delta_k) \frac{\partial \phi^{\text{PM}}}{\partial r^k}, \quad (\text{C.5})$$

<sup>7</sup>Our expansion is different from that in Ref. [9], where  $\phi^{\text{PM}}(\mathbf{x})$  is expanded in  $1 + \Delta_i - \sqrt[3]{1 + \Delta_0}$ .

and

$$\begin{aligned}
\frac{\partial \phi^{\text{PM}}}{\partial r^k} = & -\frac{Gm}{2a\sqrt{\pi}x_s} \left[ \frac{r_k}{r} I_3'(r) + \frac{r_k}{r} \sum_i \left( -I_5'(r) + \frac{r_i^2}{2a^2x_s^2} I_7'(r) \right) \Delta_i + \frac{r_k}{a^2x_s^2} I_7(r) \Delta_k \right. \\
& + \frac{1}{2} \frac{r_k}{r} \sum_i \left( -I_5'(r) + \left( 3 + \frac{r_i^2}{2a^2x_s^2} \right) I_7'(r) - \frac{3r_i^2}{a^2x_s^2} I_9'(r) + \frac{r_i^4}{4a^4x_s^4} I_{11}'(r) \right) \Delta_i^2 \\
& + \left( \frac{r_k}{2a^2x_s^2} I_7(r) - \frac{3r_k}{a^2x_s^2} I_9(r) + \frac{r_k^3}{2a^4x_s^4} I_{11}(r) \right) \Delta_k^2 \\
& + \frac{1}{2} \frac{r_k}{r} \sum_{i \neq j} \left( I_7'(r) - \frac{r_i^2 + r_j^2}{2a^2x_s^2} I_9'(r) + \frac{r_i^2 r_j^2}{4a^4x_s^4} I_{11}'(r) \right) \Delta_i \Delta_j \\
& \left. + \Delta_k \sum_{i \neq k} \left( -\frac{r_k}{2a^2x_s^2} I_9(r) + \frac{r_i^2 r_k}{4a^4x_s^4} I_{11}(r) \right) \Delta_i \right], \tag{C.6}
\end{aligned}$$

where  $I_k'(r)$  is the derivative of  $I_k(r)$  given by

$$I_k'(r) = \frac{\partial I_k(r)}{\partial r} = \frac{2}{r} \left[ \exp\left(-\frac{r^2}{4a^2x_s^2}\right) - \frac{k-2}{2} \left(\frac{r}{2ax_s}\right)^{2-k} \gamma\left(\frac{k-2}{2}, \frac{r^2}{4a^2x_s^2}\right) \right]. \tag{C.7}$$

## D Comparison between our simulation and the conventional separate universe simulation

In this appendix, we show the result of the convergence test for the isotropic background by comparing our simulations with the conventional separate universe simulations.

### D.1 Recap of the usual separate universe simulations

One way to incorporate the isotropic super-box mode is to change the background parameters according to its value. This technique is based on the fact that the flat FLRW universe with the spherically homogenous density perturbation  $\Delta_0$  is equivalent to the curved FLRW universe without  $\Delta_0$ . This means  $\Delta_0$  can be absorbed into the background parameters in cosmological simulations. The relation of cosmological parameters between the global and local universe can be characterized by the ratio of Hubble parameters,

$$\delta h \equiv \frac{h_W}{h} = \sqrt{1 - \frac{3}{5} \frac{\Omega_m}{D(t_0)} \Delta_0^{(1)}(t_0)}, \tag{D.1}$$

where  $h_W$  is the local Hubble parameter and hereafter the subscript  $W$  denotes local quantities. In terms of  $\delta h$ , other cosmological parameters are given by

$$\Omega_{mW} = \Omega_m \delta h^{-2}, \tag{D.2}$$

$$\Omega_{\Lambda W} = \Omega_\Lambda \delta h^{-2}, \tag{D.3}$$

$$\Omega_{KW} = 1 - \delta h^{-2}. \tag{D.4}$$

In general, the time and comoving coordinates are also different among the global and local universes. Each cosmology has its own expansion history and thus  $a_W \neq 1$  when  $a = 1$ .

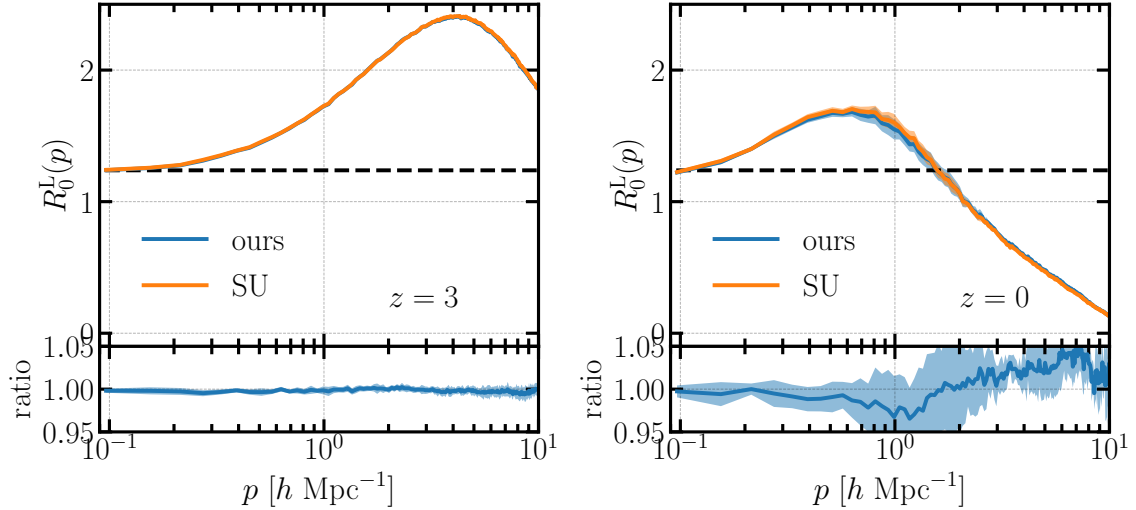


**Figure 8:** *Upper panel:* Power spectrum responses to the large-scale overdensity ( $\Delta_0$ ) from our simulations (blue) and usual separate universe (SU) simulations (orange) at  $z = 0$  and 3. The horizontal dashed line presents the tree-level prediction of the perturbation theory (Eq. (4.7)). *Lower panel:* the ratio of the two: ours/SU.

Therefore we need to find the relation between the global and local scale factors at the same physical time  $t$ . We can compute the difference between  $a_W$  and  $a$  by numerically solving Eq. (2.12) with  $\tau_i = 0$ , since the difference of the Friedmann equations in the two cosmology solves the spherical collapse. We have to be careful to this mapping of time in generating the initial conditions and determining the output time.

As for the comoving length, it is common to use the unit of  $\text{Mpc}/h$  so the simulation box are given by  $L \text{ Mpc}/h$  and  $L_W \text{ Mpc}/h_W$  in each cosmology. The choice of  $L_W$  depends on what one wants to measure directly from separate universe simulations. If one needs to obtain the Eulerian response directly,  $L_W$  is set to follow  $a_W(t_{\text{out}})L_W/h_W = a(t_{\text{out}})L/h$  with  $t_{\text{out}}$  being the output physical time. In order to get the Lagrangian response directly, one have to set  $L_W/h_W = L/h$ . The former and the latter is called as the total derivative method and the growth-dilation method respectively in Ref. [1]. We employ the growth-dilation method where we set  $L_W/h_W = L/h$  at all times to share the random fluctuations in the comoving scale in  $\text{Mpc}$ .

In this comparison study, we ran 6 pairs of separate universe simulations with  $\Delta_0^{(1)} = \pm 0.09$ . The boxsize is  $L = 250 \text{ Mpc}/h$  and the number of particles is  $N_p = 1024^3$ , which are the same as our high-resolution simulations.

## D.2 Power spectrum response

This subsection presents the comparison of the power spectrum response to the density perturbation  $\Delta_0$  from both our  $N$ -body simulation and 2LPT with that from the usual separate universe simulations. We estimate  $R_0^L(p)$  as

$$R_0^L(p, z) = \frac{P_W(p, z; \Delta_0^{(1)} = +\epsilon) - P_W(p, z; \Delta_0^{(1)} = -\epsilon)}{2\epsilon D(z)P(p)}. \quad (\text{D.5})$$

### D.2.1 Convergence of $N$ -body results

Fig. 8 shows the  $R_0^L(p)$  responses from our simulations and the usual separate universe simulations. For both  $z = 3$  and  $z = 0$ , our results are in good agreement with the usual separate universe one, down to  $k \simeq 10 h/\text{Mpc}$ .

### D.2.2 On the valid scale of our 2LPT at high redshifts

Here we discuss the valid scales of our 2LPT by comparing it with the separate universe  $N$ -body results. Fig. 9 presents the  $R_0^L(p)$  responses at  $z = 15$ , 10, and 7 from our 2LPT and the usual separate universe simulations. Note that the boxsize of our 2LPT is  $L = 100 \text{ Mpc}/h$  with  $N_p = 1024^3$  while the usual separate universe simulations have  $L = 250 \text{ Mpc}/h$  with  $N_p = 1024^3$ . Setting the criteria to be 5% difference between our 2LPT and the separate universe simulations, we conclude the responses from our 2LPT are reliable up to  $k = 9$ , 4, and  $2h/\text{Mpc}$  at  $z = 15$ , 10, and 7, respectively.

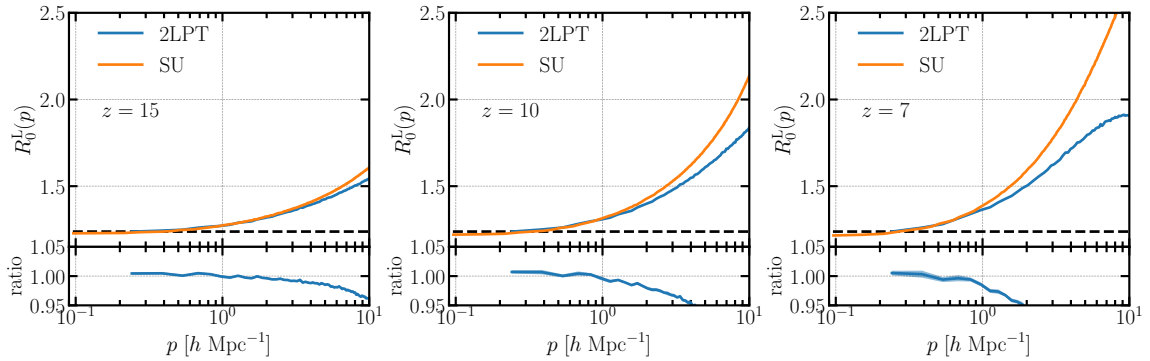


**Figure 9:** *Upper panel:* Power spectrum responses to the large-scale overdensity ( $\Delta_0$ ) from our modified 2LPT (blue) and usual separate universe (SU) simulations (orange) at  $z = 15$ , 10, and 7. *Lower panel:* the ratio of the two: 2LPT/SU.

### D.3 Linear bias

Finally we also compare results on the linear bias measured from our simulations and the separate universe simulations. First, we directly measure the Lagrangian linear bias  $b_1^L$  as

$$b_1^L(M, z) = \frac{N_h(M, z; \Delta_0^{(1)} = +\epsilon) - N_h(M, z; \Delta_0^{(1)} = -\epsilon)}{2\epsilon D(z) N_h(M, z; \Delta_0^{(1)} = 0)}, \quad (\text{D.6})$$

where  $N_h(M, z)$  is the total number of halos at mass  $M$  in the local comoving volume. Then the Eulerian linear bias is computed as  $b_1^E = b_1^L + 1$ . Fig. 10 shows  $b_1^E$  at  $z = 0$  and 2. For all mass range our results agree with those from the usual separate universe simulations. Together with the results about  $R_0^L(p)$ , this suggests that our implementation is correctly working.

## E Results from the inertial tensor $I_{ij}$

In this appendix, we summarize the shape response results when using the inertial tensor  $I_{ij}$ . Fig. 11a shows the boxsize or equivalently resolution dependence of  $b_K$ . Unlike using  $J_{ij}$ , there is no difference between  $b_K$  at 6th and 7th mass-bin from  $L = 250 \text{ Mpc}/h$  and

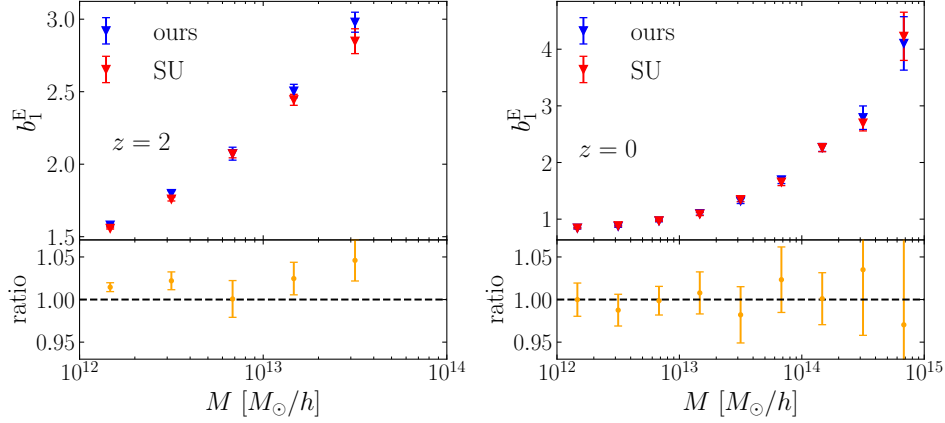


**Figure 10:** *Upper panel:*  $b_1^E$  from our simulations (blue) and usual separate universe simulations (red). *Lower panel:* the ratio of the two: ours/SU.

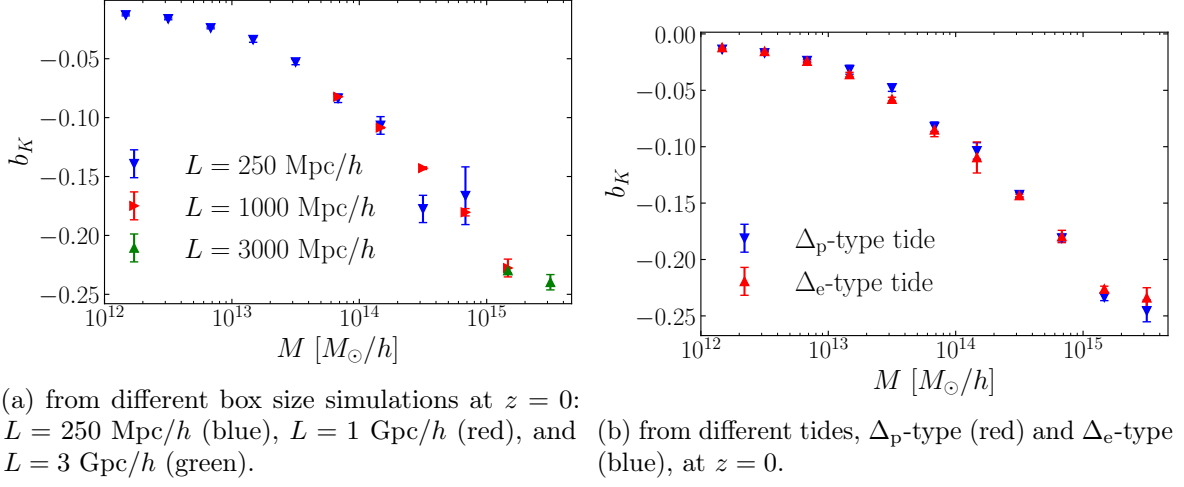
$L = 1$  Gpc/h. This can be explained by the enough number of particle to determine the halo shape when using  $J_{ij}$  in 1 Gpc/h simulations since the number of particles used to define the the halo shape is effectively higher in  $I_{ij}$  than in  $J_{ij}$ . Given these results, in the following in this appendix we use 250 Mpc/h, 1 Gpc/h, and 3 Gpc/h simulations for 1st-6th, 7th-9th, and 10th-11th mass-bin, respectively.

Fig. 11b compares  $b_K$  from different kinds of tides and Fig. 12 shows the time evolution of  $b_K$  when using  $I_{ij}$ . While the amplitude of  $b_K$  from  $I_{ij}$  differs from  $J_{ij}$ ,  $I_{ij}$  results show the same trend as  $J_{ij}$ . The universal behavior between  $b_1^E$  and  $b_K$  is also found from  $I_{ij}$  results as shown in Fig. 13. This implies that this relation is indeed “universal”, regardless of the definition of shapes. In  $I_{ij}$  case we can fit this relation as

$$b_K = \frac{0.09302 - 0.1289b_1^E}{1 + 0.3541b_1^E} \quad (\text{E.1})$$

In Fig. 14 we provide the comparison of  $b_K$  measured from  $I_{ij}$  and  $J_{ij}$  for various redshifts and mass-bins. For all points, the amplitude of  $|b_K|$  is greater when using  $I_{ij}$  than when using  $J_{ij}$  and its ratio does not change significantly over redshifts and mass-bins. Thus the choice of the definition of shapes does not change the dependence of  $b_K$  on mass or redshift as already seen in Fig. 12.

Finally, in Fig. 15 and Fig. 16, we present that the secondary dependence of  $b_K$  on halo concentration and the axis-ratio is also found when using  $I_{ij}$  with the same trend. This suggests that the secondary dependence of  $b_K$  is genuine.



**Figure 11:** Linear alignment coefficient,  $b_K$ , for the reduced inertial tensor,  $I_{ij}$

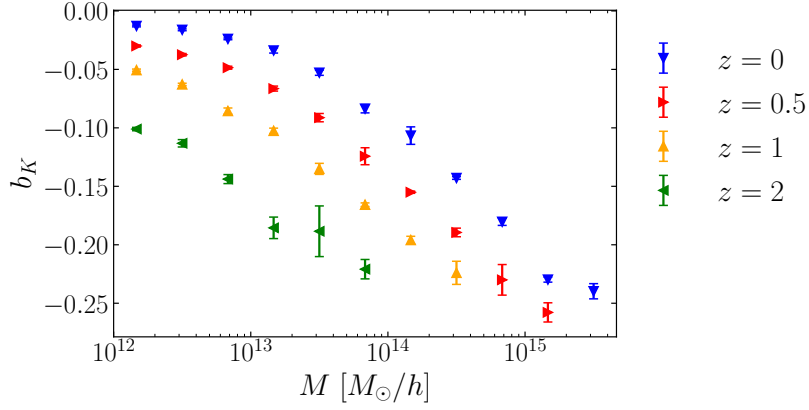


**Figure 12:** Linear alignment coefficient,  $b_K$ , for the reduced inertial tensor,  $I_{ij}$ , at various redshifts:  $z = 0$  (blue),  $z = 0.5$  (red),  $z = 1$  (orange),  $z = 2$  (green). Here we combine the results from difference boxsize and difference tides simulations.

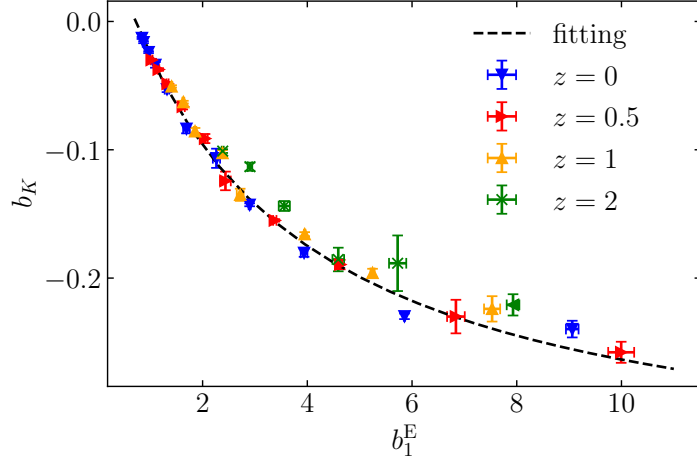


**Figure 13:** Linear alignment coefficient,  $b_K$ , from  $I_{ij}$ , as a function of the Eulerian linear bias,  $b_1^E$ , combining all redshift and mass information. The dashed curve is the fitting given in Eq. (E.1).



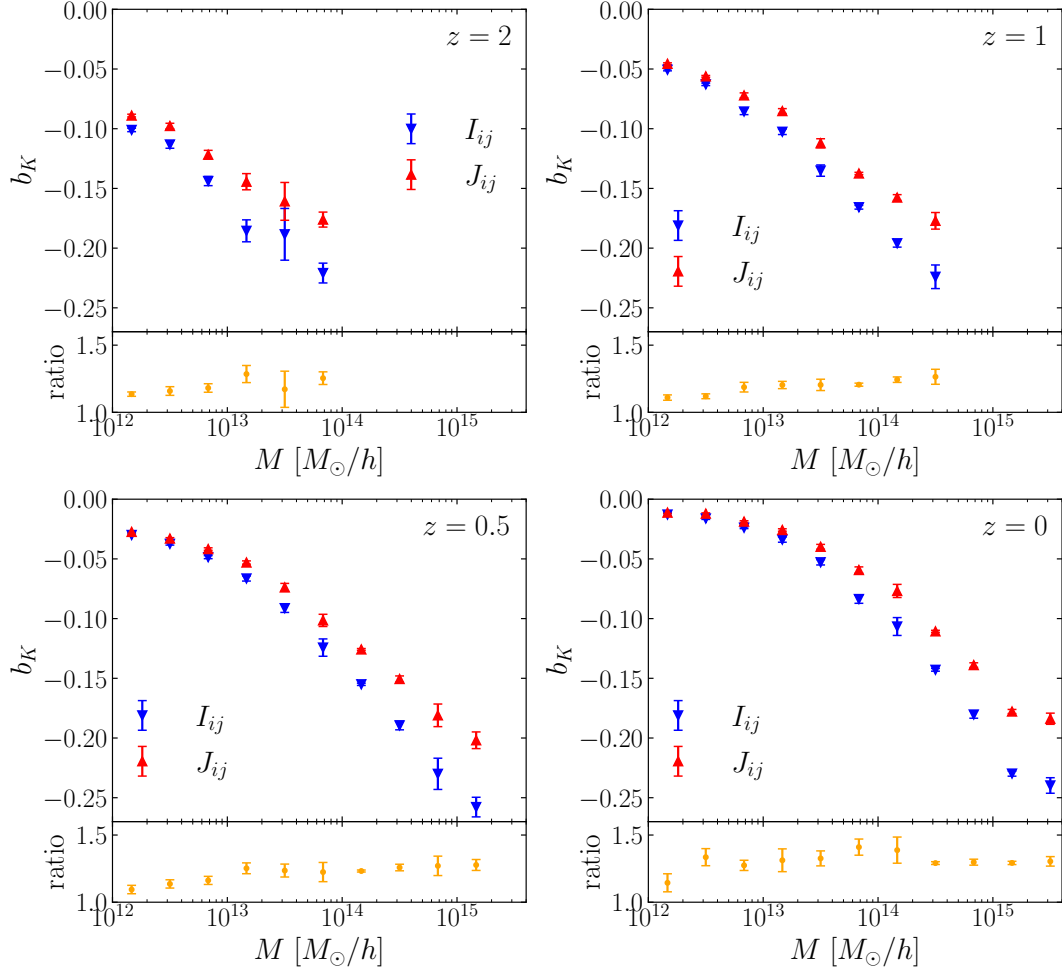


**Figure 14:** *Upper panel:* The shape definition dependence of the linear alignment coefficient,  $b_K$ , at various redshifts and masses:  $b_K$  from  $I_{ij}$  (blue) and  $J_{ij}$  (red). *Left panel:* The ratio of the two:  $I_{ij}/J_{ij}$ .

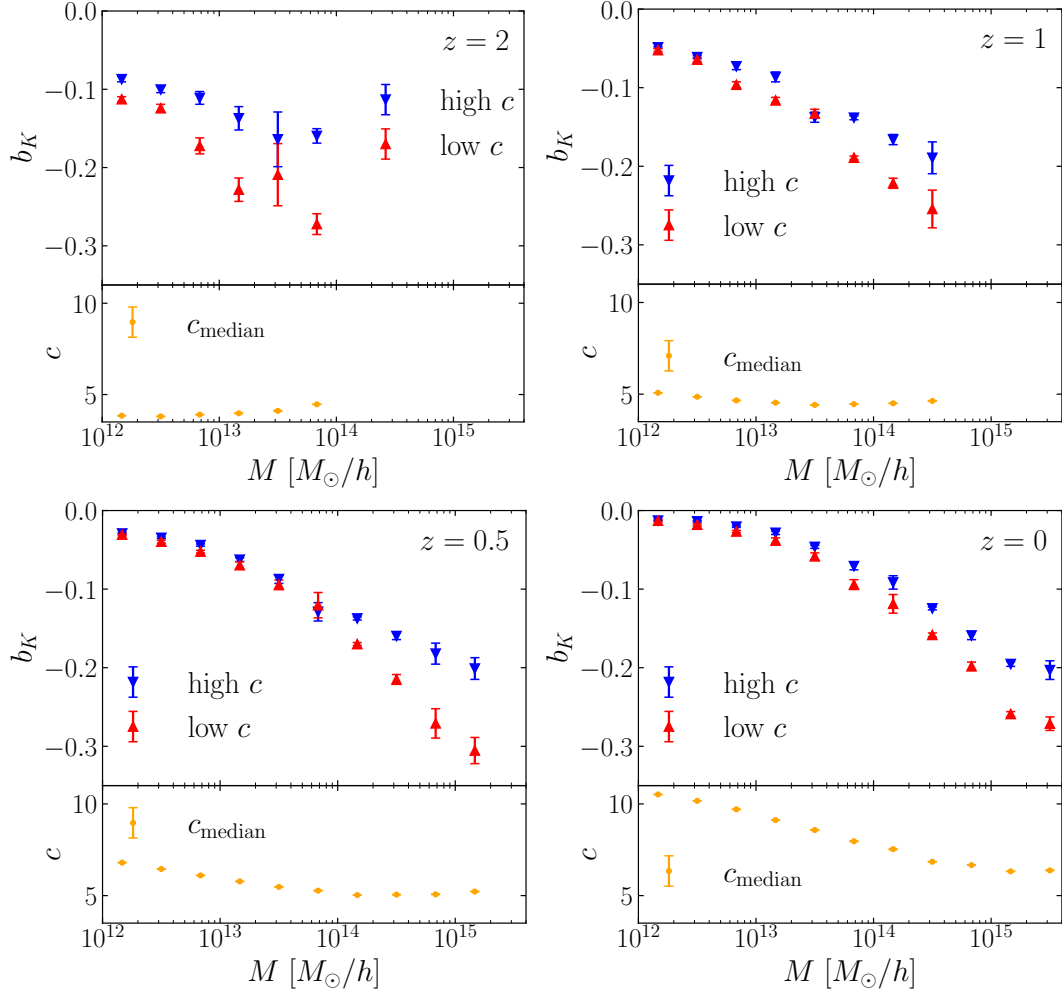


**Figure 15:** *Upper panel:* The halo concentration dependence of the linear alignment coefficient,  $b_K$ , at various redshifts and masses:  $b_K$  from high concentration (blue) and low concentration (red). *Left panel:* The median concentration on which we divided halo samples.

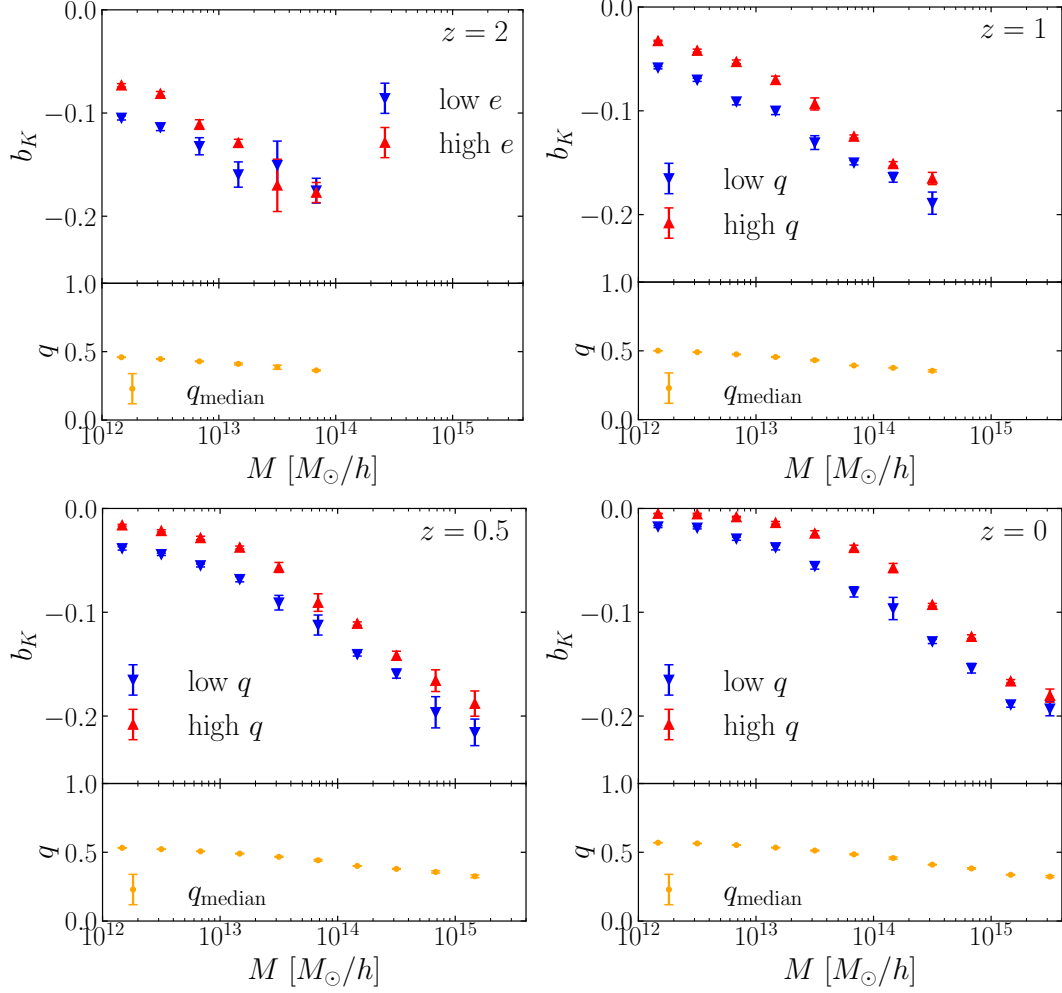


**Figure 16:** *Upper panel:* The axis-ratio ( $q = I_3/I_1$  with  $I_1 \geq I_3$ ) dependence of the linear alignment coefficient,  $b_K$ , at various redshifts and masses:  $b_K$  from high  $q$  (low ellipticity, blue) and low  $q$  (high ellipticity, red). *Left panel:* The median axis-ratio on which we divided halo samples.

## References

- [1] Y. Li, W. Hu and M. Takada, *Super-Sample Covariance in Simulations*, *Phys. Rev. D* **89** (2014) 083519 [[1401.0385](#)].
- [2] C. Wagner, F. Schmidt, C.-T. Chiang and E. Komatsu, *Separate universe simulations*, *Monthly Notices of the Royal Astronomical Society: Letters* **448** (2015) L11.
- [3] T. Baldauf, U. Seljak, L. Senatore and M. Zaldarriaga, *Linear response to long wavelength fluctuations using curvature simulations*, *JCAP* **09** (2016) 007 [[1511.01465](#)].
- [4] Y. Li, W. Hu and M. Takada, *Separate Universe Consistency Relation and Calibration of Halo Bias*, *Phys. Rev. D* **93** (2016) 063507 [[1511.01454](#)].
- [5] T. Lazeyras, C. Wagner, T. Baldauf and F. Schmidt, *Precision measurement of the local bias of dark matter halos*, *JCAP* **02** (2016) 018 [[1511.01096](#)].
- [6] J. Bond and S. Myers, *The peak-patch picture of cosmic catalogs. i. algorithms*, *The Astrophysical Journal Supplement Series* **103** (1996) 1.
- [7] K. Akitsu, M. Takada and Y. Li, *Large-scale tidal effect on redshift-space power spectrum in a finite-volume survey*, *Phys. Rev. D* **95** (2017) 083522 [[1611.04723](#)].
- [8] A.S. Schmidt, S.D. White, F. Schmidt and J. Stücker, *Cosmological N-Body Simulations with a Large-Scale Tidal Field*, *Mon. Not. Roy. Astron. Soc.* **479** (2018) 162 [[1803.03274](#)].
- [9] J. Stücker, A. Schmidt, S.D. White, F. Schmidt and O. Hahn, *Measuring the Tidal Response of Structure Formation: Anisotropic Separate Universe Simulations using TreePM*, [2003.06427](#).
- [10] S. Masaki, T. Nishimichi and M. Takada, *Anisotropic separate universe simulations*, *Mon. Not. Roy. Astron. Soc.* **496** (2020) 483 [[2003.10052](#)].
- [11] S. Masaki, T. Nishimichi and M. Takada, *Impacts of pre-initial conditions on anisotropic separate universe simulations: a boosted tidal response in the epoch of reionization*, [2007.08727](#).
- [12] K. Akitsu and M. Takada, *Impact of large-scale tides on cosmological distortions via redshift-space power spectrum*, *Phys. Rev. D* **97** (2018) 063527 [[1711.00012](#)].
- [13] Y. Li, M. Schmittfull and U. Seljak, *Galaxy power-spectrum responses and redshift-space super-sample effect*, *Journal of Cosmology and Astroparticle Physics* **2018** (2018) 022.
- [14] K. Akitsu, N.S. Sugiyama and M. Shiraishi, *Super-sample tidal modes on the celestial sphere*, *Phys. Rev. D* **100** (2019) 103515 [[1907.10591](#)].
- [15] A. Barreira, E. Krause and F. Schmidt, *Complete super-sample lensing covariance in the response approach*, *JCAP* **06** (2018) 015 [[1711.07467](#)].
- [16] P. Catelan, M. Kamionkowski and R.D. Blandford, *Intrinsic and extrinsic galaxy alignment*, *Mon. Not. Roy. Astron. Soc.* **320** (2001) L7 [[astro-ph/0005470](#)].
- [17] C.M. Hirata and U. Seljak, *Intrinsic alignment-lensing interference as a contaminant of cosmic shear*, *Phys. Rev. D* **70** (2004) 063526 [[astro-ph/0406275](#)].
- [18] R. Mandelbaum, C.M. Hirata, M. Ishak, U. Seljak and J. Brinkmann, *Detection of large scale intrinsic ellipticity-density correlation from the sloan digital sky survey and implications for weak lensing surveys*, *Mon. Not. Roy. Astron. Soc.* **367** (2006) 611 [[astro-ph/0509026](#)].
- [19] A. Taruya and T. Okumura, *Improving geometric and dynamical constraints on cosmology with intrinsic alignments of galaxies*, [2001.05962](#).
- [20] T. Kurita, M. Takada, T. Nishimichi, R. Takahashi, K. Osato and Y. Kobayashi, *Power spectrum of halo intrinsic alignments in simulations*, [2004.12579](#).
- [21] F. Schmidt and D. Jeong, *Large-Scale Structure with Gravitational Waves II: Shear*, *Phys. Rev. D* **86** (2012) 083513 [[1205.1514](#)].

- [22] F. Schmidt, E. Pajer and M. Zaldarriaga, *Large-Scale Structure and Gravitational Waves III: Tidal Effects*, *Phys. Rev. D* **89** (2014) 083507 [[1312.5616](#)].
- [23] F. Schmidt, N.E. Chisari and C. Dvorkin, *Imprint of inflation on galaxy shape correlations*, *JCAP* **10** (2015) 032 [[1506.02671](#)].
- [24] K. Akitsu, T. Kurita, T. Nishimichi, M. Takada and S. Tanaka, *Imprint of anisotropic primordial non-Gaussianity on halo intrinsic alignments in simulations*, [2007.03670](#).
- [25] K. Kogai, K. Akitsu, F. Schmidt and Y. Urakawa, *Galaxy imaging surveys as spin-sensitive detector for cosmological colliders*, [2009.05517](#).
- [26] N.Y. Gnedin, A.V. Kravtsov and D.H. Rudd, *Implementing the DC Mode in Cosmological Simulations with Supercomoving Variables*, *Astrophys. J. Suppl.* **194** (2011) 46 [[1104.1428](#)].
- [27] B.D. Sherwin and M. Zaldarriaga, *Shift of the baryon acoustic oscillation scale: A simple physical picture*, *Physical Review D* **85** (2012) 103523.
- [28] Y.B. Zel'Dovich, *Gravitational instability: An approximate theory for large density perturbations.*, *Astronomy and astrophysics* **5** (1970) 84.
- [29] M. Crocce, S. Pueblas and R. Scoccimarro, *Transients from initial conditions in cosmological simulations*, *MNRAS* **373** (2006) 369 [[astro-ph/0606505](#)].
- [30] J.S. Bagla, *TreePM: A Code for Cosmological N-Body Simulations*, *Journal of Astrophysics and Astronomy* **23** (2002) 185 [[astro-ph/9911025](#)].
- [31] J.S. Bagla and S. Ray, *Performance characteristics of TreePM codes*, *New A* **8** (2003) 665 [[astro-ph/0212129](#)].
- [32] T. Quinn, N. Katz, J. Stadel and G. Lake, *Time stepping N-body simulations*, *ArXiv Astrophysics e-prints* (1997) [[astro-ph/9710043](#)].
- [33] V. Springel, S.D. White, A. Jenkins, C.S. Frenk, N. Yoshida, L. Gao et al., *Simulations of the formation, evolution and clustering of galaxies and quasars*, *nature* **435** (2005) 629.
- [34] Planck Collaboration, P.A.R. Ade, N. Aghanim, M. Arnaud, M. Ashdown, J. Aumont et al., *Planck 2015 results. XIII. Cosmological parameters*, *A&A* **594** (2016) A13 [[1502.01589](#)].
- [35] D. Blas, J. Lesgourgues and T. Tram, *The cosmic linear anisotropy solving system (class). part ii: approximation schemes*, *Journal of Cosmology and Astroparticle Physics* **2011** (2011) 034.
- [36] S.R. Knollmann and A. Knebe, *Ahf: Amiga's halo finder*, *The Astrophysical Journal Supplement Series* **182** (2009) 608.
- [37] T. Okumura, Y.P. Jing and C. Li, *Intrinsic Ellipticity Correlation of SDSS Luminous Red Galaxies and Misalignment with Their Host Dark Matter Halos*, *ApJ* **694** (2009) 214 [[0809.3790](#)].
- [38] A. Faltenbacher, C. Li, S.D.M. White, Y.-P. Jing, Shu-DeMao and J. Wang, *Alignment between galaxies and large-scale structure*, *Research in Astronomy and Astrophysics* **9** (2009) 41 [[0811.1995](#)].
- [39] T. Okumura and Y.P. Jing, *The Gravitational Shear-Intrinsic Ellipticity Correlation Functions of Luminous Red Galaxies in Observation and in the  $\Lambda$ CDM Model*, *ApJ* **694** (2009) L83 [[0812.2935](#)].
- [40] J. Shi, T. Kurita, M. Takada, K. Osato, Y. Kobayashi and T. Nishimichi, *Power Spectrum of Intrinsic Alignments of Galaxies in IllustrisTNG*, *arXiv e-prints* (2020) arXiv:2009.00276 [[2009.00276](#)].
- [41] D.M. Schmitz, C.M. Hirata, J. Blazek and E. Krause, *Time evolution of intrinsic alignments of galaxies*, *JCAP* **07** (2018) 030 [[1805.02649](#)].

- [42] F. Prada, A.A. Klypin, A.J. Cuesta, J.E. Betancort-Rijo and J. Primack, *Halo concentrations in the standard  $\lambda$  cold dark matter cosmology*, *Monthly Notices of the Royal Astronomical Society* **423** (2012) 3018.
- [43] N. Dalal, M. White, J. Bond and A. Shirokov, *Halo Assembly Bias in Hierarchical Structure Formation*, *Astrophys. J.* **687** (2008) 12 [[0803.3453](#)].
- [44] A. Obuljen, N. Dalal and W.J. Percival, *Anisotropic halo assembly bias and redshift-space distortions*, *JCAP* **10** (2019) 020 [[1906.11823](#)].
- [45] A. Obuljen, W.J. Percival and N. Dalal, *Detection of anisotropic galaxy assembly bias in BOSS DR12*, *JCAP* **10** (2020) 058 [[2004.07240](#)].